

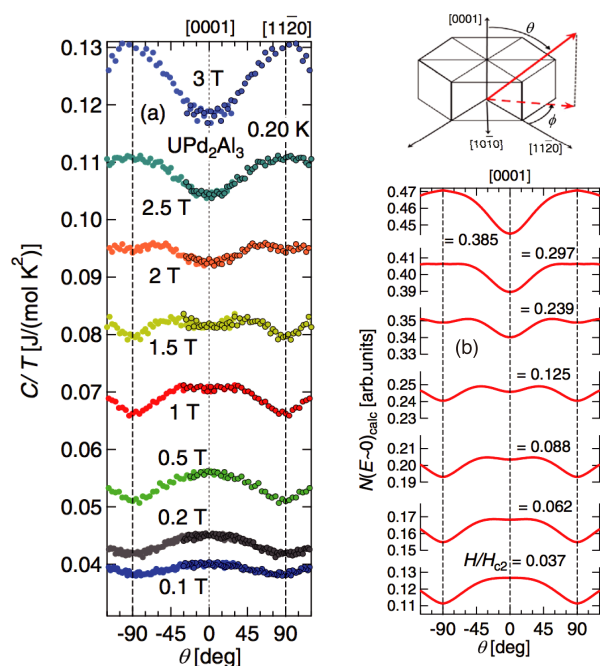
Research Highlights

Identification of the Superconducting Gap Structure of the Heavy-Fermion Antiferromagnet UPd₂Al₃ by Angle-Resolved Heat Capacity Measurements

Sakakibara Group

The hexagonal heavy-fermion compound UPd₂Al₃ exhibits superconductivity below $T_c = 2$ K, which coexists with an antiferromagnetic ordering that sets in at $T_N = 14.5$ K [1]. Various experiments including inelastic neutron scattering [2] and thermal conductivity [3] measurements have inferred that the superconducting gap function is of nodal A_{1g} type, $\Delta(k) = \Delta_0 \cos(k_z c)$, having horizontal line nodes. Up to present, however, no thermodynamic evidence for the horizontal line node has been obtained.

In order to examine the pairing symmetry of UPd₂Al₃ in the light of quasiparticle density of states, we performed angle-resolved heat capacity (C) measurements on a high quality single crystal of UPd₂Al₃ in rotating magnetic fields (H) [4]. When H is rotated in the basal plane, no angular variation of $C(H, \phi)$ that could be ascribed to vertical line nodes is observed. To probe the horizontal line node, we examined the polar-angle (θ) dependence $C(H, \theta)$ and the results are shown in Fig. 1(a). Below 0.5 T, a twofold oscillation is clearly observed with a maximum at $\theta = 0^\circ$ ($H \parallel [0001]$) and a minimum at $\theta = 90^\circ$ ($H \parallel [11\bar{2}0]$). Above



(a) Field-angle variation of $C(H, \theta)/T$ of UPd₂Al₃ with H rotated in the ac plane measured at 0.2 K. (b) Calculated results of the field-angle dependence of ZEDOS in magnetic fields normalized by H_{c2} for a linear horizontal line node. The inset shows the definition of angles for the hexagonal structure.

2.5 T, the twofold angular oscillation is reversed and the maximum appears along $[11\bar{2}0]$, reflecting the underlying nodal structure as well as the anisotropy of the upper critical field H_{c2} . Very interestingly, in the field range from 1 to 2 T, a new feature appears in $C(H, \theta)$ in an intermediate angle region; at 1 T, a shoulder or a hump appears at $\theta \sim 30^\circ$, and moves to the higher angle side $\theta \sim 45^\circ$ - 60° with increasing H to 2 T. Above 2.5 T, it finally merges into the maximum at $\theta = 90^\circ$ arising from the H_{c2} anisotropy. Remarkably, the maximum of $C(H, \theta)/T$ at 1.5 T occurs near 45° .

The observed field evolution of $C(H, \theta)$, in particular the shoulder/hump structure in the intermediate angular region, provides strong evidence that a horizontal line node exists on the Fermi surface. We performed microscopic calculations of the zero-energy density of states (ZEDOS) by means of the quasiclassical Eilenberger theory within the Kramer-Pesch approximation [4]. Figure 1(b) shows the calculated angular dependence of ZEDOS, assuming a spherical Fermi surface and a model gap function $\Delta(k) = \Delta_0 k_z$ that has a horizontal line node at the equator. The results clearly demonstrate that the anisotropy inversion occurs in the ZEDOS as H increases. What is more important is that the calculated results successfully reproduce the shoulder/hump anomaly around 30° - 60° in $C(H, \theta)$ at the intermediate fields. The polar angle dependence of $C(H, \theta)$, therefore, possesses sufficiently high resolution to detect the horizontal line node.

References

- [1] C. Geibel *et al.*, Z. Phys. B Condens. Matt. **84**, 1 (1991).
- [2] N. Bernhoeft *et al.*, Phys. Rev. Lett. **81**, 4244 (1998).
- [3] T. Watanabe *et al.*, Phys. Rev. B **70**, 184502 (2004).
- [4] Y. Shimizu *et al.*, Phys. Rev. Lett. **117**, 037001 (2016).

Authors

Y. Shimizu, S. Kittaka, T. Sakakibara, Y. Tsutsumi^a, T. Nomoto^b, H. Ikeda^c, K. Machida^c, Y. Homma^d, and D. Aoki^d

^aUniversity of Tokyo

^bKyoto University

^cRitsumeikan University

^dTohoku University

Improved Stability of a Metallic State in Benzothienobenzothiophene (BTBT)-based Molecular Conductors: an Effective Increase of Dimensionality with Hydrogen Bonds

Mori Group

One of the merits in organic conductors based upon molecules is the designability and variety of molecular components [1], which lead a wide range of electronic states such as exotic metallic [2], superconducting [3], Dirac Fermion, quantum spin liquid [4], and electron glass states. These curious solid states [2-6] have been given a birth based

upon newly designed and synthesized molecules, usually tetrathiafulvalene (TTF) and its derivatives with 7 π system. Recently, another donor molecule benzothienobenzothiophene (BTBT) with 6 π system has been synthesized to be a superior semiconductor for field-effect-transistor. Although this BTBT is poor electron donor, it is realized to afford one-dimensional molecular conductor, (BTBT)₂PF₆. In this article, the successfully improved stability of a metallic state in newly synthesized BTBT derivative-based molecular conductor, β -[BTBT(OH)₂]₂ClO₄, by the increase of dimensionality with hydrogen (H)-bonds is reported [6].

The novel donor molecule BTBT(OH)₂ was synthesized by 7 steps with utilizing Sonogashira coupling method. Surprisingly, our newly synthesized BTBT(OH)₂ functionalized at the 2,3-positions has been unknown, although a lot of BTBT derivatives have been designed and synthesized so far. Therefore, our present synthetic strategy will be effective in exploring a new class of functionalized BTBT derivatives. The electrocrystallization of BTBT(OH)₂ in the presence of tetra-*n*-butylammonium perchlorate gave the molecular conductor, needle-like black crystals of the ClO₄ salt, namely β -[BTBT(OH)₂]₂ClO₄. The BTBT(OH)₂ is partially oxidized state with a +0.5e charge and expected to form a 3/4-filled band structure. The BTBT(OH)₂ molecule is almost planar and forms a head-to-tail-type uniform stack along the *b*-axis with an inter-planar spacing of 3.326 Å. It is noteworthy that two kinds of [O–H...O]-type H-bonding interactions were observed between the hydroxy groups of the donor and the ClO₄ anion. Consequently, an infinite 1D H-bond-chain structure is formed along the *c*-axis. In this arrangement, very weak C–H...S interactions are also found in the side-by-side direction of the donor molecule. As a result of these intermolecular interactions, BTBT(OH)₂ produces a sheet type molecular arrangement (Fig. 1). The transfer integrals, which correspond to inter-molecular interactions between the neighbouring molecules, are largest in the stacking direction *b* (91.0 meV) and relatively smaller in the diagonal directions *p* (2.77 meV), *q* (13.6 meV), and *r* (13.1 meV). The effect of the H-bond interactions in the crystal of β -[BTBT(OH)₂]₂ClO₄ is further disclosed by comparing the

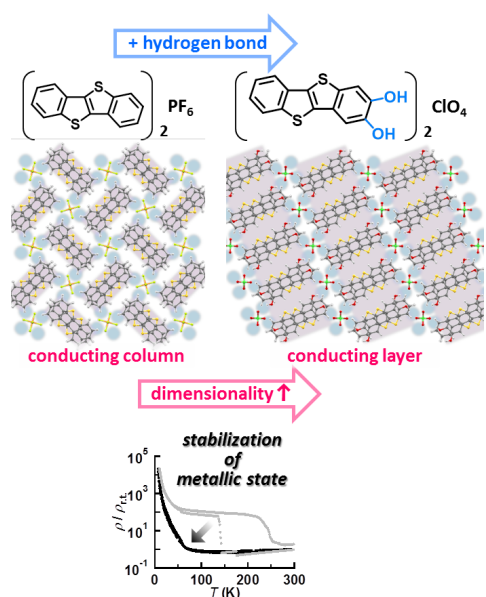


Fig. 1. We have proved that hydrogen-bonding interaction can increase the dimensionality and stabilize a metallic state for the newly synthesized benzothienobenzothiophene (BTBT)-based molecular conductor, β -[BTBT(OH)₂]₂ClO₄. This charge-transfer complex offers a new promising strategy for designing and developing next generation organic electronic materials/devices.

crystal structures of β -[BTBT(OH)₂]₂ClO₄ and the parent salt (BTBT)₂PF₆. As shown in Fig. 1, the BTBT molecules in (BTBT)₂PF₆ form windmill-type columnar structures with effective π - π interactions. There are however, no effective interactions between the columns, due to the existence of C–H...F contacts between the donor molecule and the PF₆ anion. As a result, the columnar arrangement produces a typical 1D electronic structure with a flat Fermi surface. On the other hand, the π -stacking columns in the present salt β -[BTBT(OH)₂]₂ClO₄ (Fig. 1) are connected with the O–H...O H-bonding interactions through the ClO₄ anions. The resultant Fermi surface is warped in the 3/4-filled band structure, which means the formation of a quasi-one-dimensional (Q1D) electronic structure in β -[BTBT(OH)₂]₂ClO₄. This enhancement of the electronic structure from 1D to Q1D is also evidenced by comparing the anisotropy of the transfer integrals. (BTBT)₂PF₆ has a strong interaction within the π -stacking column (87 meV); however, the inter-stack interaction is negligibly small (1.4 meV). On the other hand, the present β -[BTBT(OH)₂]₂ClO₄ has the substantial interstack interactions (*q*, *r* \sim 13 meV), in addition to the strong intrastack one (*b* = 91 meV), as described before. Thus, the intrastack/interstack anisotropy is significantly decreased from 60 (= 87/1.4) in (BTBT)₂PF₆ to 7 (= 91/13) in β -[BTBT(OH)₂]₂ClO₄.

The increase of the dimensionality of the electronic structure significantly influenced the electrical conducting properties. The crystal of β -[BTBT(OH)₂]₂ClO₄ shows a relatively low room temperature electrical resistivity (ρ_{300K} = 5.5×10^{-3} ohm cm), which decreases with decreasing temperature down to 135 K. This temperature dependence indicates that this salt is metallic above 135 K, and more importantly, this metallic state is more stable than that of (BTBT)₂PF₆. This is because this salt does not show an abrupt resistivity jump, as seen in (BTBT)₂PF₆ at 150 K. Therefore, we have proved that the increase of the dimensionality caused by the H-bond interactions brings about the stabilization of the metallic state in BTBT-based conductors. On further cooling, this salt finally undergoes a metal–insulator-like transition around 60 K, after entering the semiconducting state at 135 K. A similar transition without hysteresis has also been observed in (BTBT)₂PF₆ at around 50 K.

In conclusion, we have successfully synthesized novel organic donor with 6 π system and the introduction of hydrogen bond, benzothienobenzothiophene (BTBT) derivative, BTBT(OH)₂, and realized a stable metallic state in a quasi-one dimensional charge-transfer salt, β -[BTBT(OH)₂]₂ClO₄. The strong H-bonding ability of the catechol-type hydroxyl groups has played a crucial role in the formation of an infinite one-dimensional H-bonded chain structure, which leads to the increase of the dimensionality of the electronic structure and the stable metallic state. These results demonstrate that functionalized BTBT derivatives are promising electron donors in molecular conductors. We believe that this study will pave a new way for designing and developing high-dimensional BTBT-based materials/devices with interesting conducting properties (e.g. superconductivity and high carrier mobility).

References

- [1] H. Kamo, A. Ueda, T. Isono, K. Takahashi, and H. Mori, *Tetrahedron Lett.* **53**, 4385 (2012).
- [2] T. Isono, H. Kamo, A. Ueda, K. Takahashi, A. Nakao, R. Kumai, H. Nakao, K. Kobayashi, Y. Murakami, and H. Mori, *Nature Commun.* **4**, 1344 (2013).
- [3] S. Kimura, R. Chiba, T. Mori, T. Kawamoto, H. Mori, H. Moriyama, Y. Nishio, and K. Kajita, *Chem. Commun.* **2004**, 2454.

- [4] T. Isono, H. Kamo, A. Ueda, K. Takahashi, M. Kimata, H. Tajima, S. Tsuchiya, T. Terashima, S. Uji, and H. Mori, *Phys. Rev. Lett.* **112**, 177201 (2014).
 [5] A. Ueda, S. Yamada, T. Isono, H. Kamo, A. Nakao, R. Kumai, H. Nakao, Y. Murakami, K. Yamamoto, Y. Nishio, and H. Mori, *J. Am. Chem. Soc.* **136** (34), 12184 (2014).
 [6] T. Higashino, A. Ueda, J. Yoshida, and H. Mori, *Chem. Commun.* **53**, 3426 (2017).

Authors

T. Higashino, A. Ueda, J. Yoshida, and H. Mori

Double Carrier Transport in Electron-Doped Region in High-Mobility Thin-Film Black Phosphorus FET

Osada Group

Black phosphorus (BP) is a layered material which was extensively studied in the 1980s because it was a single-element semiconductor with higher mobility than silicon or germanium. In the past a few years, BP has again attracted a great deal of attention as one of post-graphene atomic layer materials. It shows high performance as a field effect transistor (FET) material; much larger on/off ratio than graphene and higher mobility than transition metal dichalcogenides. It is known that thin-film BP is degraded by photochemical reaction under oxygen and water atmosphere, so that techniques to avoid the degradation are important to obtain high quality thin films. Using high quality samples, the Shubnikov-de Haas (SdH) oscillations and the quantum Hall effect of two dimensional (2D) carriers have been studied. However, most of preceding studies were performed in negatively gated (hole-doped) region. In this work, we have achieved the highest Hall mobility ever reported in thin-film BP, and observed clear SdH oscillations, which indicate double carrier transport in positively gated (electron-doped) region.

The samples were prepared by the mechanical exfoliation and dry transfer techniques in the glove box to avoid degradation. First, a thin-film BP flake with the thickness of 15-20 nm is fixed on an atomically-flat hexagonal boron nitride (h-BN) flake on the $\text{SiO}_2/\text{n}^+\text{-Si}$ substrate. Next, it is partially covered by a smaller h-BN flake. Electrodes are formed on the edge of this top h-BN flake by the lithography process in the atmosphere. Since the measured region in BP layer is sandwiched by two h-BN layers, we can avoid the degradation and improve carrier mobility. Using this simple method, we have achieved the Hall mobility of $6,000 \text{ cm}^2/\text{Vs}$ and $5,800 \text{ cm}^2/\text{Vs}$ at 4.2 K for holes and electrons, respectively. These values are comparable to the reported highest mobility.

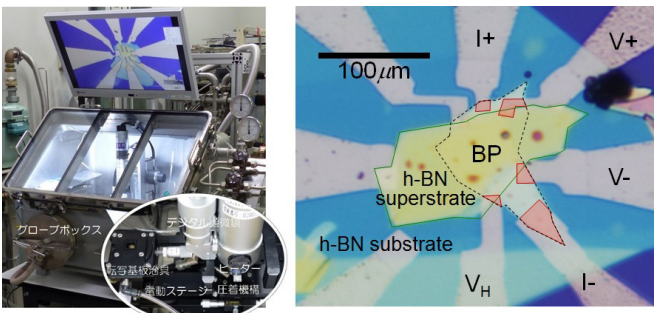


Fig. 1. (left) Exfoliation and transfer system for building atomic layer heterostructures. (right) Microscope image of thin-film BP FET device.

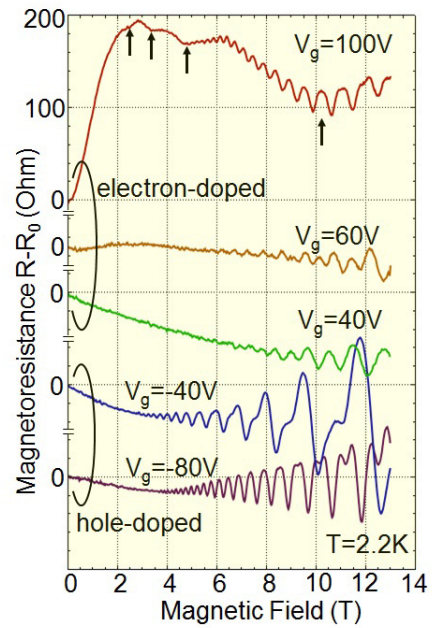


Fig. 2. Magnetoresistance of thin-film BP FET under several gate voltages.

In the negatively-gated (hole-doped) side, we have observed negative magnetoresistance (MR) due to weak localization and SdH oscillations with clear spin splitting. The carrier density estimated from the SdH period is well proportional to the gate voltage with small correction of charge neutrality. This fact indicates that a single 2D hole gas is formed in the inversion layer.

In contrast, anomalous transport behaviors have been observed in the positively gated (electron-doped) side. The gate voltage dependence of conductance showed an anomalous shoulder structure. In the gate voltages below it, normal behaviors, the negative MR and single SdH oscillation, were observed like the hole-doped side. In the gate voltages above it, the MR turned to positive and saturated accompanied by slow and fast SdH oscillations. The summation of carrier densities estimated from two SdH periods coincides with the density expected from the gate voltage. These facts clearly suggest the existence of two closed Fermi surfaces. In addition, the overall shape of MR can be qualitatively explained by the two carrier model.

The appearance of the second Fermi surface in high positive gate voltages is explained by the carrier population onto the second subband. In thin-film BP FETs, the 3D conduction band splits into 2D subbands due to finite thickness and strong gate electric field. Since the present BP sample is rather thick (15-20 nm), the subband separation is considered to be small, so that electrons easily populate on the second subband. The present result demonstrates to control the subband configuration by the gate voltage in BP FETs.

Authors

T. Osada, K. Hirose, K. Uchida, T. Taen, K. Watanabe^a, T. Taniguchi^a, and Y. Akahama^b

^aNational Institute for Material Science

^bUniversity of Hyogo

Spin Singlet Orders in Breathing Pyrochlores

Tsunetsugu Group

Geometrically frustrated magnets are a good playground in the quest for new quantum phases of matter, and kagome and pyrochlore magnets are their representatives. A few years ago, Okamoto *et al.* [1] discovered an unidentified phase transition in the spinel variety $\text{Li}(\text{Ga},\text{In})\text{Cr}_4\text{O}_8$, in which the magnetic Cr ions form a breathing pyrochlore lattice, and this has motivated a theoretical investigation of its origin.

The breathing pyrochlore lattice is a staggered network of corner-sharing tetrahedrons with two sizes, and increasing In concentration enhances the size difference. The antiferromagnetic Heisenberg Hamiltonian is a minimal model to study magnetic properties in this compound, and this requires two values of nearest-neighbor exchange coupling $J' \ll J$ corresponding to different tetrahedron units. This model was theoretically studied for the case of spin $S = 1/2$ [2] and it was predicted that the spin gap is finite and the ground state exhibits a complicated spatial modulation without breaking spin rotation symmetry. Among the four sublattices of small tetrahedra, three of them show dimer-pair orders of different pairing combination, and the remaining sublattice shows either a dimer-pair order or a tetramer order. Considering Cr^{3+} ions have a spin $S = 3/2$, the important issue is if this larger spin changes an order in the ground state.

To study this problem, I have developed a systematic scheme of degenerate perturbation theory for the breathing pyrochlore Heisenberg model with general spin S , and derived an effective Hamiltonian for describing dynamics in the spin singlet subspace. The effective Hamiltonian is in the order of $(J'/J)^3$ and represented in terms of spin-pair operators τ , and we have studied its ground state by a mean field approximation [3]. The operators are defined in the local singlet space with dimension $2S + 1$ at each small tetrahedron, and we have solved the challenge of calculating their matrix elements for general S . It turns out that an essential difference from the $S = 1/2$ case is the presence of Z_3 anisotropy in the internal τ space, and this stabilizes a different order. The anisotropy grows for larger S and inherits the cubic symmetry of the lattice structure. Two sublattices of small tetrahedrons now show an identical tetramer order, and the other two sublattices show another tetramer order with a

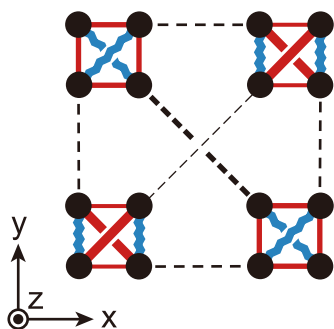


Fig. 1. Nearest-neighbor spin correlations in the breathing-pyrochlore Heisenberg model with $S = 3/2$. Four squares depict small tetrahedron units in the cubic unit cell projected onto the xy plane. In each unit, antiferromagnetic correlations are shown by red bonds and their width schematically shows $|S_i \cdot S_j|$, while blue bonds show ferromagnetic correlations. Dashed lines show weak antiferromagnetic correlations between neighboring units.

small distortion. We have analyzed the spin correlations in this new ordered state in detail for $S = 3/2$ and 1, and calculated the equal-time spin structure factor $S(\mathbf{q})$. The amplitudes of the components breaking the cubic lattice symmetry in $S(\mathbf{q})$ are calculated and they can be used to determine the value of J'/J . It shall be interesting to verify this scenario by carrying out a neutron scattering experiment and compare its results with this prediction.

References

- [1] Y. Okamoto, G. Nilsen, T. Nakazono, and Z. Hiroi, J. Phys. Soc. Jpn. **84**, 043707 (2015).
- [2] H. Tsunetsugu, J. Phys. Soc. Jpn. **70**, 640 (2001); Phys. Rev. B **65**, 024415 (2001).
- [3] H. Tsunetsugu, Prog. Theor. Exp. Phys. **2017**, 033101 (2017).

Author

H. Tsunetsugu

Supercurrent in a Ferromagnetic Semiconductor

Katsumoto Group

The origin of superconductivity is the pairing of two electrons (Cooper pairing). In conventional superconductors such a pairing occurs between electrons with opposite spins and momentums at the Fermi surface. The total spin of a conventional Cooper pair is, thus zero (spin-singlet pairing). There may exist, however, another type of pairing with total spin one, that is, spin-triplet pairing. A solid example is the pairing of two helium-3 atoms in the state of superfluidity. Many exotic properties are predicted for spin-triplet (odd parity) superconductivity though few of them have been experimentally confirmed. Spin-triplet superconductivity may appear in non-uniform superconductivities such as proximity driven superconductivity in a half-metallic ferromagnetic material, in which only a single spin state exists at the Fermi level. In this study, we have made a diluted ferromagnetic semiconductor (In, Fe)As [1] superconducting by placing Nb split electrodes with gaps around $1 \mu\text{m}$. The magnetic field dependence of the critical current suggests that the spin-triplet pairing is presumably realized in (In, Fe)As.

The (In, Fe)As film was grown in Tanaka laboratory in Department of Electrical Engineering and Communication Technology, University of Tokyo by molecular beam epitaxy.

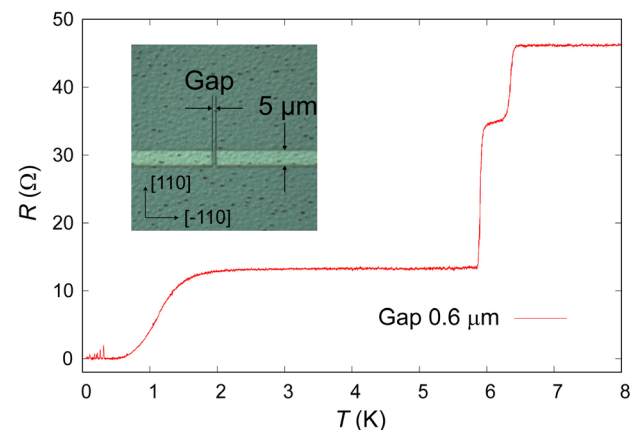


Fig. 1. Two-terminal resistance of a Nb-(In, Fe)As-Nb junction as a function of the temperature. The inset shows optical micrographs of the sample, which consists of $5 \mu\text{m}$ wide Nb strips and $0.6 \mu\text{m}$ width gap of (In, Fe)As.

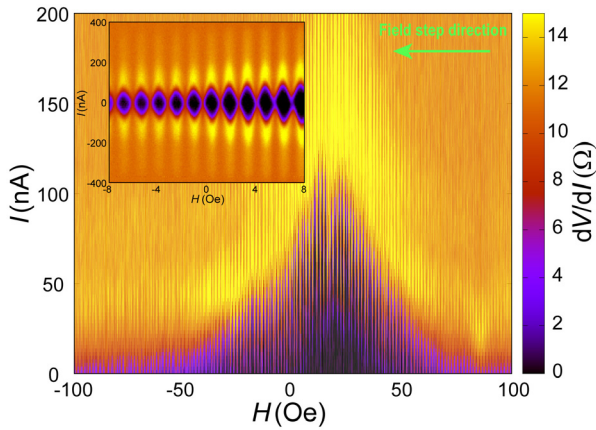


Fig. 2. Differential resistance of the sample shown in Fig.1 is plotted in color as a function of the perpendicular magnetic field and the device current. The inset is a blowup around the origin, which shows clear diamond-like zero-resistance regions. The green arrow indicates the direction of the field sweep.

As shown in the inset, Nb strips with the width 5 μm were deposited leaving the gap of 0.6 μm as shown in the inset of Fig. 1. Figure 1 displays the temperature dependence of the sample resistance, which have a two-step drop at the transition temperature of Nb. Below 1.5 K, the resistance decreases again with decreasing temperature and reaches zero around 0.5 K. In Fig. 2, we plot the differential resistance in color as a function of the perpendicular magnetic field and the device current. A Fraunhofer-like interference pattern with a very short period in magnetic field appears with a shifted broad peak. The period much shorter than that for single flux quantum in the junction area comes from flux concentration by the Nb electrodes.

A peculiar point is that the peak position exists on the positive side of zero magnetic field while the field is swept from positive to negative. For the opposite sweep direction, the peak position appears on the negative side. This means the critical current is affected by hysteretic magnetization of the ferromagnet. Then why the peak is formed for high magnetic flux position? The key is magnetic disorder at the interface between (In, Fe)As and Nb. The peak always exists when the disorder is maximized, which fact suggests the spin-triplet pairing is realized in ferromagnetic (In,Fe)As.

Reference

[1] M. Tanaka, S. Ohya, and P. Nam Hai, Appl. Phys. Reviews 1, 011102 (2014).

Authors

T. Nakamura, L. D. Anh^a, S. Ohya^a, M. Tanaka^a, and S. Katsumoto^a

^aThe University of Tokyo

Tuning the Spin Hall Effect of Pt from the Moderately Dirty to the Superclean Regime

Otani Group

Spintronics research relies on the techniques of spin currents generation and detection. Therefore the discovery of the spin Hall effect was one of the most important breakthrough in this area, which enabled us to interconvert between charge and spin currents without using ferromagnets. Thanks to the discovery, spin Seebeck effect [1] and spin pumping [2] have been demonstrated successfully.

The SHE was theoretically predicted by Dyakonov and Perel in 1971 [3] and revisited by Hirsch in 1999 [4]. It is

widely recognized that the SHE in nonmagnetic materials shares the same mechanism with the anomalous Hall effect (AHE) in ferromagnets; either intrinsic or extrinsic mechanism. In case of the AHE, experiments with changing the longitudinal conductivity of ferromagnetic metals have been performed, showing that the intrinsic and extrinsic contributions scale differently with the longitudinal conductivity. In contrast to the AHE, however, a systematic experimental study on the SHE has been still lacking.

We have studied on the spin diffusion length λ_{Pt} and the spin Hall angle $\theta_{\text{SH,Pt}}$ (conversion yield between spin and charge currents) of platinum in a wide range of conductivities σ_{Pt} by means of the spin absorption method using lateral spin valve devices [5]. Pt was chosen because it is a prototypical SHE metal so that our results can be compared with many reported values. Also there have been a discussion on the values of λ_{Pt} and $\theta_{\text{SH,Pt}}$ because the value differ in each report where λ_{Pt} ranges from 1~10 nm and $\theta_{\text{SH,Pt}}$ from 1~10 % [6]. A linear relation between λ_{Pt} and σ_{Pt} was firstly observed as shown in Fig. 1, evidencing that the spin relaxation in Pt is governed by the Elliott-Yafet (EY) mechanism. Also, we decomposed intrinsic and extrinsic contri-

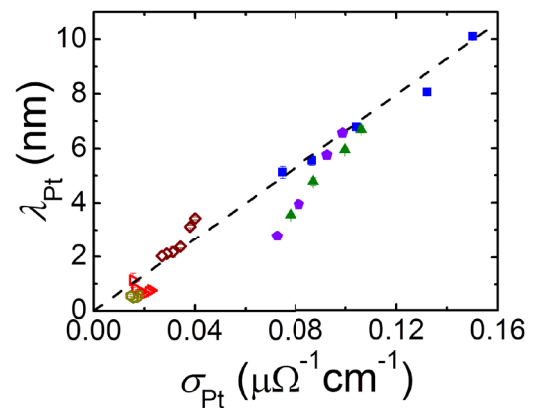


Fig. 1. Spin diffusion length λ_{Pt} of Pt depending on the longitudinal conductivity σ_{Pt} . Each symbol shows a different sample which is measured in various temperatures. The black dashed line is the linear fitting. This linearity is evidencing that the spin relaxation mechanism in Pt is governed by Elliot-Yafet mechanism. The obtained variation of the spin diffusion length λ_{Pt} covers the values in the previous researches.

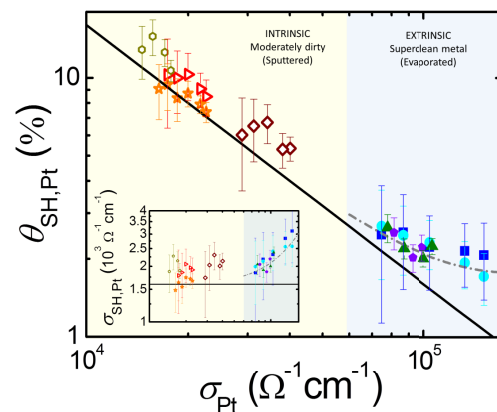


Fig. 2. Spin Hall angle $\theta_{\text{SH,Pt}}$ of Pt depending on the longitudinal conductivity σ_{Pt} . The inset shows the Spin Hall conductivity $\sigma_{\text{SH,Pt}}$ of Pt depending on the longitudinal conductivity σ_{Pt} . Each symbol shows a different sample which is measured in various temperatures. The black solid line is a guide to the eye which express the inverse proportional relation between $\theta_{\text{SH,Pt}}$ and σ_{Pt} when you consider only intrinsic mechanism. The purple dashed line is the corrected line from the black solid one with considering extrinsic contribution. On the left part (Moderately dirty region) the behavior of the $\theta_{\text{SH,Pt}}$ is well explained only by intrinsic contribution. On the other hand on the right part (Superclean region) $\theta_{\text{SH,Pt}}$ gradually differ from the black line and extrinsic contribution become more dominant.

butions for each sample by analyzing the data measured in different temperatures. We found a single intrinsic spin Hall conductivity ($\sigma_{SH}^{int} = 1540 \pm 100 \Omega^{-1} \text{cm}^{-1}$), that is the material's characteristic value, for Pt in all the studied range of σ_{Pt} , being in good agreement with the theoretical value [7]. By collecting all the data in our study, we have obtained for the first time the crossover from the intrinsic regime (moderately dirty) to the extrinsic one (super-clean) in the SHE by changing the quality of Pt as shown in Fig. 2, equivalent to that for the AHE. Our results explain the wide dispersion in previously reported values of λ_{Pt} and $\theta_{SH,Pt}$, and show a route to maximize the spin Hall angle. The smaller is σ_{Pt} (dirtier Pt), the larger will be $\theta_{SH,Pt}$.

References

- [1] K. Uchida, J. Xiao, H. Adachi, J. Ohe, S. Takahashi, J. Ieda, T. Ota, Y. Kajiwara, H. Umezawa, H. Kawai, G. E. W. Bauer, S. Maekawa, and E. Saitoh, *Nat. Mater.* **9**, 894 (2010).
- [2] E. Saitoh, M. Ueda, H. Mikajima, and G. Tatara, *Appl. Phys. Lett.* **88**, 182509 (2006).
- [3] M. I. Dyakonov and V. I. Perel, *Phys. Lett. A* **35**, 459 (1971).
- [4] J. E. Hirsch, *Phys. Rev. Lett.* **83**, 1834 (1999).
- [5] E. Sagasta, Y. Omori, M. Isasa, M. Gradhand, L. E. Hueso, Y. Niimi, Y. Otani, and F. Casanova, *Phys. Rev. B* **94**, 060412(R) (2016).
- [6] J. Sinova, S. O. Valenzuela, J. Wunderlich, C. H. Back, and T. Jungwirth, *Rev. Mod. Phys.* **87**, 1213 (2015).
- [7] T. Tanaka, H. Kontani, M. Naito, T. Naito, D. S. Hirashima, K. Yamada, and J. Inoue, *Phys. Rev. B* **77**, 165117 (2008).

Authors

Y. Omori, and Y. Otani

Epitaxial Fcc Iron Thin Film Stabilized via Strain Relief from Steps

Komori Group

In hetero-epitaxially grown thin films where designed electronic and magnetic properties can be sustained, an appropriate choice of the substrate is crucial to keep the matching of the lattice symmetry and constant. However, transformation of the crystal structure from the epitaxial one

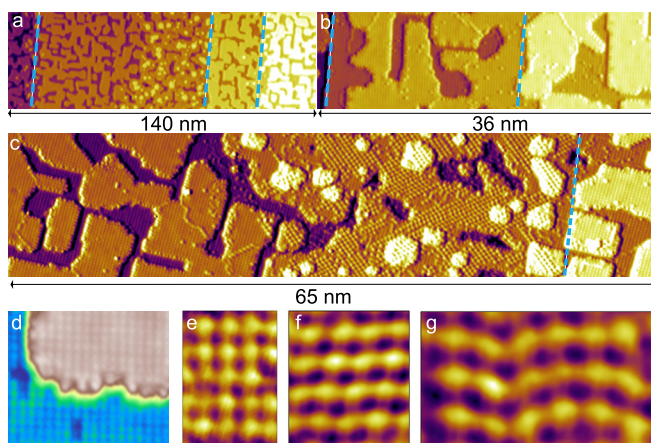


Fig. 1. STM images of the surface of an Fe film grown on a vicinal Cu(001) surface. Dotted lines indicate substrate step edges. (a) Image including three steps. (b) High-resolution image indicating growth of an fcc Fe film with a square surface lattice on a narrow terrace. Large protrusions on the terrace are adsorbed CO atoms. (c) High-resolution image indicating growth of both the fcc Fe film and an Fe film with complicated surface structure on a wide terrace. On the surface of lower terrace, the right region has a square lattice, and the left complicated lattices. About 80 % of the latter surface is covered by CO atoms forming local 2×2 structures. (d) Magnified image of the fcc Fe surface. (e-g) Magnified images of the left region in (c) with adsorbed CO atoms. Square (e), $p2mg(2 \times 1)$ (f) and, nano-martensitic (g) lattices are recognized.

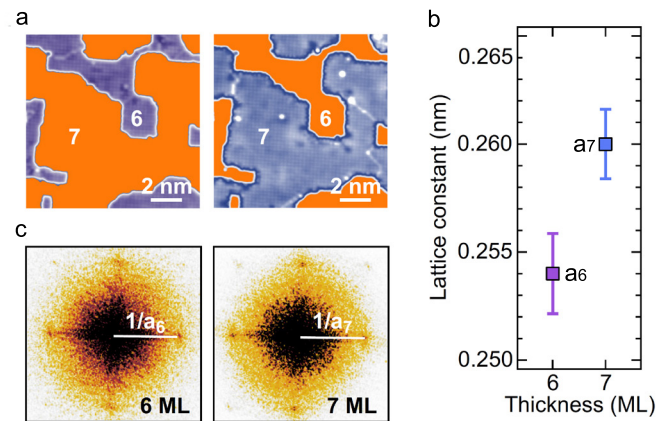


Fig. 2. (a) Atomically-resolved STM images in the fcc region with masked (left) 7 and (right) 6 ML thick Fe films. (b) FFTs of the images in (a). (c) The values of the surface lattice constant, a_6 and a_7 , extracted from different STM images of the 6 and 7 ML fcc Fe films. The error bars represent the standard deviations.

to the bulk stable one with increasing the film thickness often disturbs the characterization and uses of intrinsic electronic and magnetic properties of the epitaxially-stabilized phases. We have found that high-density steps on a vicinal Cu(001) substrate can stabilize the epitaxial fcc Fe overlayer against transformation towards the bulk stable bcc phase with increasing the coverage [1]. Here, the steps serve as strain relievers for stabilizing the epitaxial film. The fcc Fe phase has experimentally and theoretically attracted a great interest over two decades because of its complex magnetic structures. The growth on a flat Cu(001) substrate are well defined in previous studies [2], and the structural transformation from fcc to bcc Fe is implied by the appearance of the surface reconstruction [3].

Figure 1 shows STM images of the surface of a Fe film on the Cu(001) surface. The average Fe thickness is 6.9 ML. The narrow terrace consists of 6 and 7 ML thick films and the surface atoms make a square lattice as in Figs. 1(a,b,d), indicating growth of the fcc Fe film. Each wide terrace has two regions; one is the same as the narrow terrace, and the other consists of 6, 7 and 8 ML thick films with complicated surface lattices with $\sim 80\%$ coverage of adsorbed CO atoms as in Figs. 1(a,c,e,f,g). The latter region, where small areas of fcc(001), $p2mg(2 \times 1)$, nano-martensitic and bcc(110) lattices are seen, is found always at the lower side terrace of the atomic step. The width of the fcc Fe region increases with increasing the terrace width. This suggests the strain-relief due to the step edge stabilizes the fcc film even 7 ML thick.

The strain relief due to the step edge was directly confirmed using surface atomic images as in Fig. 2. On the fcc region, the surface lattice constant of the 7 ML film is $\sim 2.4\%$ larger than that of the 6 ML film. The difference of the local electronic states observed by atomic-layer resolved scanning tunneling spectroscopy was attributed to that of the lattice constant [1].

References

- [1] T. Miyamachi *et al.*, *Phys. Rev. B* **94**, 045439 (2016).
- [2] H. L. Meyerheim *et al.*, *Phys. Rev. Lett.* **103**, 267202 (2009).
- [3] A. Biedermann *et al.*, *Surf. Sci.* **563**, 110 (2004).

Authors

T. Miyamachi, S. Nakashima, S. Kim, N. Kawamura^a, Y. Tatetsu^b, Y. Gohda^{b,c}, S. Tsuneyuki^b, and F. Komori^a
^aScience & Technology Research Laboratories, NHK,
^bThe University of Tokyo
^cTokyo Institute of Technology

Step Conductivity Measured with the Proximity-Induced Superconducting Pair Correlation

Hasegawa and Kato Groups

The recent discovery of monolayer (ML) superconductivity revived the research on one-atom-thick metal layers formed on semiconductor surfaces. Electronically decoupled from the substrate, the metallic overlayers hold an ultimately-thin two-dimensional (2D) electron system, and combined with the broken inversion symmetry, they exhibit various fascinating features, such as Rashba spin-split surface states and valley spin polarized states. For these 2D systems, atomic steps on the substrate, whose presence is ubiquitous and unavoidable, play a significant role in the transport. Usually, for the characterization of electrical conductivity, an electrical current is injected from one side of the object and the transmitted one is detected in the other side. It is, however, technically very difficult to measure transport on such nano-scale structures. Here, we report on microscopic measurements of the electrical conductivity through a single ML-high step on a 2D metallic layer by inducing the superconducting pair correlation through the proximity effect, and by detecting its signal in tunneling spectra measured by scanning tunneling microscopy and spectroscopy (STM/STS).

The propagation of the pair correlation from a superconductor / normal metal (SN) interface into the normal metal has been investigated by using STM/STS. Near the interface in the normal metal, the single particle spectrum shows a dip at the Fermi energy (E_F), which is a good measure of the superconducting pair correlation. Through spatial mapping of the density of states (DOS) at E_F with nanometer spatial resolution, one can learn how the pair correlation is distributed in the normal metal. In general, the pair correlation decays with distance from the SN interface. By placing a

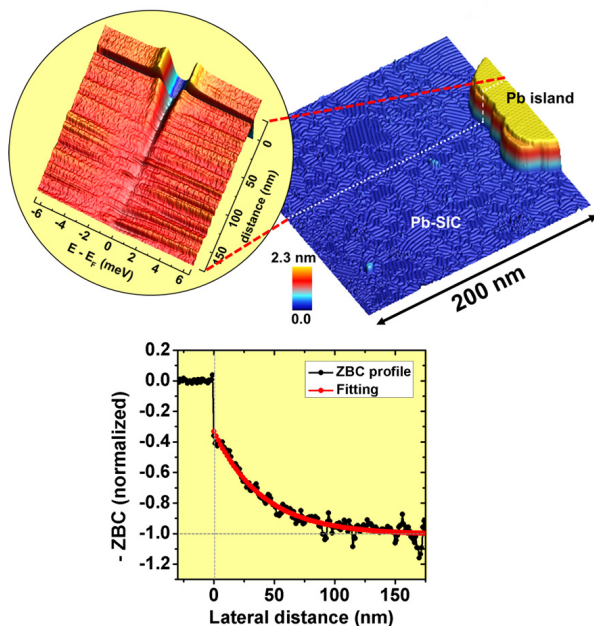


Fig. 1. (upper panel) 3D-rendered STM image showing an interface between an 8-ML Pb island and a SIC phase formed on a Si(111) substrate. A characteristic striped pattern can be seen in the SIC phase. (inset) Color-coded 200 tunneling spectra taken along the line from the Pb island to the SIC phase. (lower panel) ZBC profile around the SN interface. The red line is a fitted exponential function with the decay length of 40.5 nm.

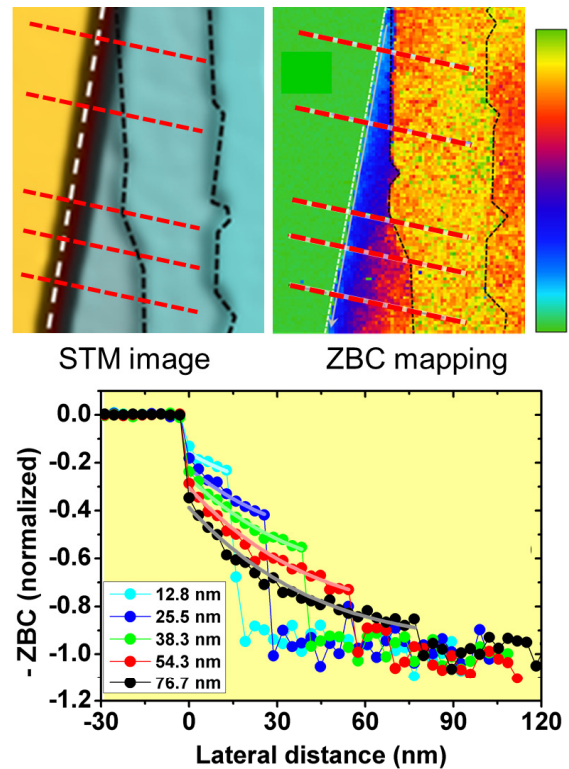


Fig. 2. (upper left) STM image of a Pb island formed on a SIC-phase-covered Si(111) substrate. The edges of the Pb islands and the steps of the SIC phase are highlighted with white and black dashed lines, respectively. (upper right) ZBC color map of the same area. (lower) ZBC profiles across the SN interface and the step edges measured along the red lines drawn in the STM and ZBC images. The length written on each plot is the terrace width measured along the corresponding line. The whitish-colored lines are theoretical curves calculated with the Usadel equation.

surface step within the decaying area we can investigate how the superconducting coherence is affected by the presence of steps and through the comparison with theoretical analysis we can estimate the conductivity through that.

We investigated the conductivity of a striped incommensurate (SIC) phase, a ML Pb-induced structure formed on Si(111) surface, which is a 2D normal metal at our measurement temperature (2.15 K). Figure 1 is an STM image showing an 8 ML Pb island on an SIC phase. Tunneling spectra taken along the line, shown in the inset, indicate a superconducting gap in the Pb island and no gap in the SIC phase far from the island. In the SIC phase near the island a suppressed gap, induced by the proximity effect, can be seen. The depth in the DOS at E_F , which corresponds to zero-bias conductance (ZBC), decays exponentially with distance from the interface (the decay length ~ 40 nm), as shown in the lower panel of Fig. 1. From the decay length, the conductivity through the SIC phase was estimated using the Einstein relation as $1.87 \text{ mS}/\square$. The estimated conductivity is larger than the one measured by 4-probe method ($0.77 \text{ mS}/\square$). The larger conductivity is reasonable since the separation of the 4-probe method ($20 \mu\text{m}$) is much larger than the step separation and therefore the measured area includes the steps whereas ours do not.

To measure the step conductivity, we investigated the spatial distribution of the pair correlation around steps of the normal-metal layer close to superconducting islands. The left panel of Fig. 2 is an STM image showing 22 ML high Pb island (yellow) formed on a stepped SIC phase (light blue). The ML-high steps on the SIC phase are marked with black-dashed lines. The spatial mapping of ZBC taken in the same

area is presented in the right panel of Fig. 2. In the conductance map the Pb island is colored green, which indicates zero ZBC and fully gapped superconductivity there. The 2D metallic layer far from the Pb islands is colored yellow, indicating no gap. The area surrounding the Pb islands is colored blue to red, implying a reduced DOS at E_F due to the proximity effect. Since a downward step edge is close to the island and the terrace width of the SIC area is less than the decay length, the decaying behavior of the proximity effect is strongly modified by the presence of the step edge. The bottom panel of Fig. 2 displays several cross-sectional ZBC profiles taken in the areas with various terrace widths.

In order to obtain the conductivity through the surface step we calculated the ZBC profiles using the Usadel equation and compared them with experimental results. For the calculation we considered a model composed of three regions: superconductor / normal metal / normal metal. In the model, we introduced the conductivity ratio through a step and metallic layer as a parameter. From the fitting the ratio was estimated as $10.9 \pm 3.9 \mu\text{m}^{-1}$. The ratio indicates that the contribution of the step resistance to the total surface resistance is quite significant. In the case of the stepped area shown in Fig. 2 ($\sim 90 \text{ nm}$ step separation corresponding to the tilting of 0.20°), which was observed on a nominally (111)-oriented substrate, the step resistance contributed almost 50% of the total resistance in the direction perpendicular to the step edges.

Reference

[1] H. Kim, S.-Z. Lin, M. J. Graf, Y. Miyata, Y. Nagai, T. Kato, and Y. Hasegawa, *Phys. Rev. Lett.* **117**, 116802 (2016).

Authors

H. Kim, S.-Z. Lin^a, M. J. Graf^a, Y. Miyata, Y. Nagai^b, T. Kato, and Y. Hasegawa

^aLos Alamos National Laboratory

^bJapan Atomic Energy Agency

Stability of Titania-Terminated Surfaces in Water

Lippmaa Group

Photoelectrochemical water splitting can be used to collect solar energy and generate hydrogen gas from water. While this process offers an attractive pathway to a clean energy supply, the low energy conversion efficiency presents several challenging unsolved materials science problems. One of the requirements for a suitable photoelectrode material is long-term stability in water during an electrochemical reaction. Titanium oxides such TiO_2 and SrTiO_3 are two examples of water-stable oxide semiconductors that have been widely studied in this context. However, even for well-ordered single crystal surfaces, it is difficult to determine to what extent the electrochemical reaction affects the composition or structure of the photoelectrode surface.

The purpose of this work was to analyze the oxide electrode surface stability and the oxide-water interface structure by numerical simulations and the measurement of surface hydrophilicity, atomic-scale surface morphology, and the local water density. SrTiO_3 (001) single crystals with a $(\sqrt{13} \times \sqrt{13})$ -R33.7° surface reconstruction were used for the experimental work. This surface is terminated by a partial TiO_2 double layer (Fig. 1a) that is chemically stable in water and the presence of the reconstruction pattern can

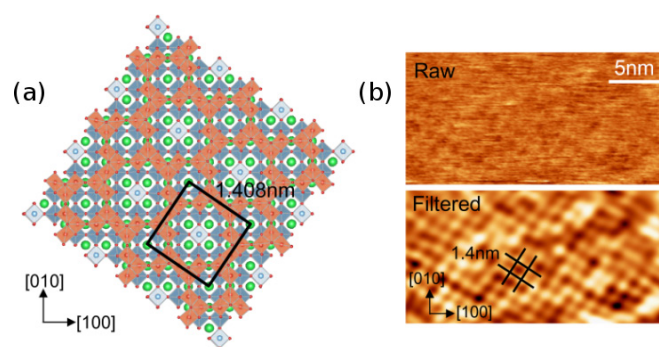


Fig. 1. (a) Surface model of the SrTiO_3 ($\sqrt{13} \times \sqrt{13}$) surface. Top layer Ti is shown in orange, second layer Ti in blue, Sr in green and O in red. (b) Raw and filtered FM-AFM images of the reconstructed surface measured in water.

be observed either by scanning probe or electron diffraction. The reconstructed ($\sqrt{13} \times \sqrt{13}$) surface can thus function as a stability marker when a crystal is subjected to various surface treatments. If the reconstruction remains detectable after a process step, we can be sure that the surface has not been structurally altered or etched. For a typical (1 × 1) SrTiO_3 surface, it would be much harder to detect structural alterations in the topmost unit cell of the crystal. A high-resolution atomic force microscope (AFM) image of the ($\sqrt{13} \times \sqrt{13}$) surface measured in water is shown in Fig. 1b. The presence of the expected periodicity shows that the surface structure is not damaged when exposed to water.

The hydration layer structure on the ($\sqrt{13} \times \sqrt{13}$) surface was simulated by density functional theory molecular dynamics to evaluate the surface stability of various crystal surface terminations. The simulation result shown in Fig. 2a indicates that a layered water molecule configuration may be expected to exist at the surface. The presence of a structured hydration layer was verified by frequency-modulation AFM in an electrolyte solution (Fig. 2b). The AFM tip was scanned laterally over the crystal surface a height scan was recorded at each lateral point, forming a depth map of water density at the surface. Two dark bands can be seen in the AFM frequency shift map in Fig. 2b, marked with M1 and M2. The density variation matches the simulation result, indicating that a stable hydration layer forms on the reconstructed SrTiO_3 surface and no chemical etching, even on a single atomic layer scale, could be observed. The presence of the reconstructed surface was verified after water exposure by high-energy electron diffraction.

Titania surfaces are known to exhibit photoinduced hydrophilicity, where the water contact angle drops dramatically upon ultraviolet illumination of a crystal surface. The

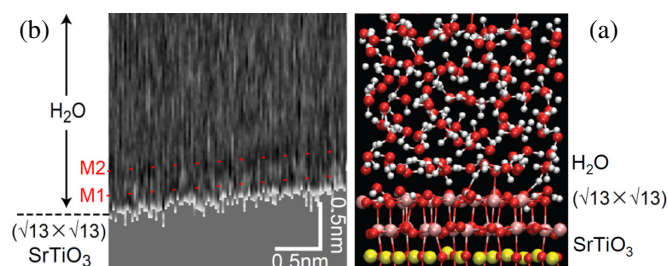


Fig. 2. (a) MD simulation of the water structure in the hydration layer above the SrTiO_3 ($\sqrt{13} \times \sqrt{13}$) surface. Sr is yellow, Ti is pink, O is red, and H is gray. (b) FM-AFM frequency shift map as a function of lateral position and distance from the surface. The local water density minima are marked M1 and M2.

hydrophilicity of the reconstructed SrTiO₃ surface was measured immediately after surface preparation in a vacuum chamber, showing that the surface is intrinsically superhydrophilic. A gradual contact angle increase occurs during several minutes of air exposure, but the superhydrophilic surface character can be regained by vacuum heating without the loss of the reconstructed surface structure. This indicates that the photoinduced hydrophilicity of the surface is related to surface contamination, rather than photoinduced structural degradation of the crystal. The work thus shows that SrTiO₃ surfaces terminated with a double TiO₂ layer are highly stable in water, even under ultraviolet exposure and can thus be used in photoelectrochemical water splitting cells that require long term electrode stability.

Reference

[1] S. Kawasaki, E. Holmström, R. Takahashi, P. Spijker, A. S. Foster, H. Onishi, and M. Lippmaa, *J. Phys. Chem. C* **121**, 2268 (2017).

Authors

S. Kawasaki, E. Holmström^a, R. Takahashi, P. Spijker^a, A. S. Foster^a, H. Onishi^b, and M. Lippmaa^a
^aAalto University
^bKobe University

Material Design of Luminescence from First-Principles

Sugino Group

Many-body Green's function methods have attracted considerable attention as emerging computational methods to allow prediction of excited states of a material from first-principles. Breakthrough was achieved by the algorithms developed for massively parallel supercomputers and by the approximations made for balancing the computational cost and accuracy. The software package developed by this group, for example, is now able to handle up to 200 atoms in a cell, sufficiently large for many applications, and provide in addition the wave function of the electron-hole pair (exciton) containing rich information of the excited states. The utilization of the exciton wave function, however, has been done infrequently, and in this context, this group proposed a method to obtain from the wave function a number of quantities that can characterize the excitons. The obtained quanti-

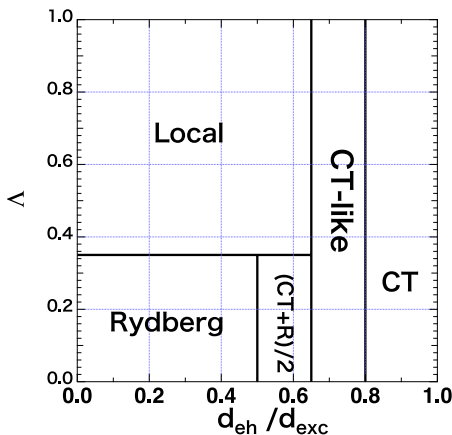


Fig. 1. Λ - d_{eh}/d_{exc} map proposed in Ref. [1] to classify excitons into local, charge-transfer (CT), Rydberg, and others such as CT-like excitons. This map has enabled to relate the exciton wave function with the characteristics of excitons, and thus relate the characteristics with the structure of a material, making it significantly easier to computationally design a luminescent material.

ties are found particularly useful in classifying the excitons into the local, charge-transfer (CT), Rydberg excitons [1], so that one may predict the luminescence dynamics induced by photoabsorption. This novel method opens possibility of a computational material design toward efficient luminescence.

The exciton wave function is a six-dimensional quantity, which has been considered to carry too prodigious amounts of information. With increasing ability of modern supercomputers, however, it has become easy to use the wave function to obtain various quantities; for example, one can calculate the exciton binding energy by taking expectation value of the electron-hole interaction operator, the electron-hole separation d_{eh} from the distance between the electron and hole, and the exciton size from the square root of the distance. When using (a) a quantity characterizing the range of the exciton Λ and (b) the electron-hole separation distance d_{eh} relative to the exciton size d_{exc} , one can plot each excited state in a two-dimensional Λ - d_{eh}/d_{exc} map (Fig. 1), wherein excitons with different type are let distribute in a different region. This method was proven useful in our subsequent study on the photoabsorption spectra of the recently synthesized cycloparaphenylene molecules [2] and on the singlet-triplet splitting of the thermally activated delayed fluorescence (TADF) molecules [3].

References

[1] D. Hirose, Y. Noguchi, and O. Sugino, *J. Chem. Phys.* **146**, 044303 (2017).
 [2] Y. Noguchi and O. Sugino, *J. Chem. Phys.* **146**, 144304 (2017).
 [3] Y. Noguchi and O. Sugino submitted to *J. Phys. Chem.*

Authors

D. Hirose, Y. Noguchi, and O. Sugino

Giant Anomalous Hall Effect in the Chiral Antiferromagnet Mn₃Ge

Nakatsuji Group

Generally, the anomalous Hall effect is known to appear in ferromagnetic conductors and is proportional to its magnetization. Recently, however, the non-collinear antiferromagnet (AFM) Mn₃Sn is found to exhibit a large anomalous Hall effect despite its vanishingly small magnetization [1]. The observation indicates that a large fictitious field or Berry curvature exists in the momentum space. The anomalous Hall effect shows a sign change upon reversal of a small magnetic field less than 0.1 T. The soft response of the

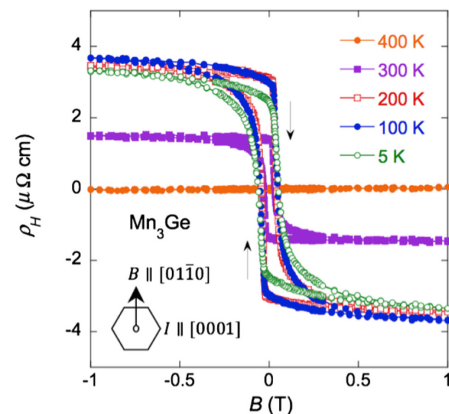


Fig. 1. Magnetic field dependence of the Hall resistivity in Mn₃Ge measured in $B//[0110]$.

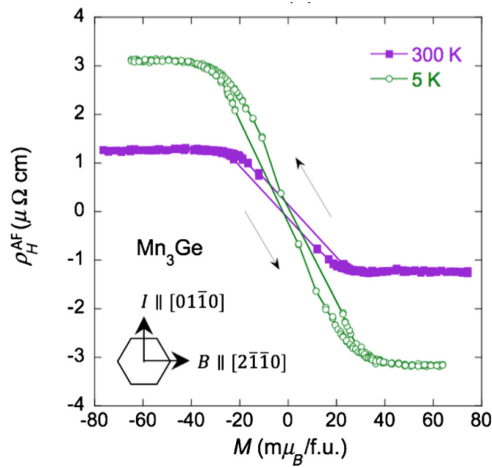


Fig. 2. Magnetization dependence of the field- and magnetization-independent part of the anomalous Hall resistivity $\rho_H^{\text{AF}} = \rho_H - R_0 B - R_3 \mu_0 M$ at 5 and 300 K.

AHE to magnetic field should be useful for applications, for example, to develop switching and memory devices based on antiferromagnets. In addition, an antiferromagnetic Weyl semimetal state is theoretically predicted by a band calculation [2]. The large AHE may well come from a significantly enhanced Berry curvature associated with the formation of Weyl points nearby the Fermi energy E_F .

Here we report another example of the AHE in a related antiferromagnet, namely, in the hexagonal chiral antiferromagnet Mn_3Ge [3]. Our single-crystal study also reveals that Mn_3Ge exhibits a giant anomalous Hall resistivity $\rho_{xz} \sim 4 \mu\Omega \text{ cm}$, corresponding to a large Hall conductivity $\sigma_{xz} \sim 60 \Omega^{-1} \text{ cm}^{-1}$, at room temperature (See Fig. 1 and 2) [4]. The advantage of the measurements for Mn_3Ge allows us to observe a giant AHE at low temperatures since Mn_3Sn has a low-temperature noncoplanar magnetic phase observed at $T < 50 \text{ K}$, where the in-plane AHE is strongly suppressed. As shown in Fig. 3, the conductivity in Mn_3Ge is enhanced with decreasing temperature without any phase transition at low temperature and shows the approximately $380 \Omega^{-1} \text{ cm}^{-1}$ at 5 K in zero field, reaching nearly half of the value expected for the quantum Hall effect per atomic layer with Chern number of unity (Fig. 3). The low temperature conductivity σ_{xz} is estimated to be three times larger than the maximum of the conductivity found in Mn_3Sn .

The observed giant AHE in the chiral antiferromagnet Mn_3Ge with a very small magnetization indicates that the

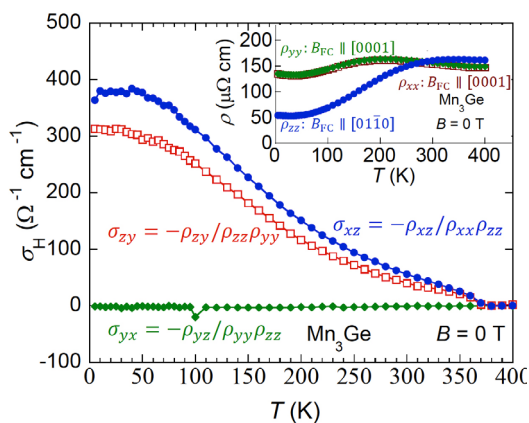


Fig. 3. Temperature dependence of the anomalous Hall effect under zero field. All the data are obtained at zero field after the field-cooling (FC) procedures made in the magnetic field B_{FC} . Directions of the field B_{FC} and electric current I used for the Hall resistivity measurements are shown in each figure.

material has a large fictitious field (equivalent to be $> 200 \text{ T}$) in the momentum space without producing almost any perturbing stray fields in the real space. The fact that the large fictitious field may be readily controlled by the application of a low external field indicates that the antiferromagnet will be useful, for example, to develop various switching and memory devices.

References

- [1] S. Nakatsuji, N. Kiyohara, and T. Higo, *Nature* **527**, 212 (2015).
- [2] H. Yang, Y. Sun, Y. Zhang, W.-J. Shi, S. S. P. Parkin, and B. Yan, *New J. Phys.* **19**, 015008 (2017).
- [3] S. Tomiyoshi, Y. Yamaguchi, and T. Nagamiya, *J. Magn. Magn. Mater.* **31–34**, 629 (1983).
- [4] N. Kiyohara, T. Tomita, and S. Nakatsuji, *Phys. Rev. Applied* **5**, 064009 (2016).

Authors

N. Kiyohara, T. Tomita, and S. Nakatsuji

Geometrically Frustrated Magnetism in the Heisenberg Pyrochlore Antiferromagnets AYb_2X_4 ($A = \text{Cd}$ and Mg , $X = \text{S}$ and Se)

Nakatsuji Group

Quantum magnetism in geometrically frustrated magnets has recently attracted great interest. In 3D systems, one of the most prominent examples is the spin ice [1], which is based on Ising spins with ferromagnetic (FM) coupling on the pyrochlore lattice. Recent studies have found that quantum melting of spin ice may lead to the formation of a quantum spin liquid state with emergent topological excitations [2]. On the other hand, various types of quantum magnetism have been discovered in the pyrochlore oxides having the non-Ising type ground Kramers doublet. An antiferromagnetic (AF) pyrochlore magnet with isotropic bilinear exchange coupling between nearest neighbor

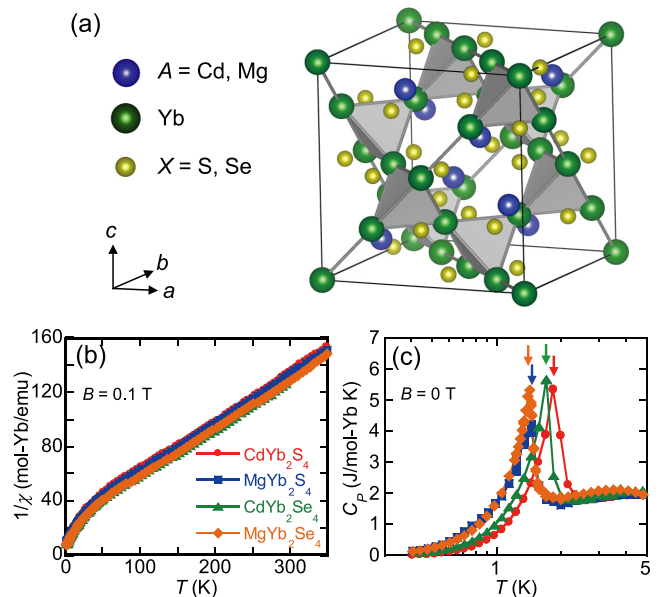


Fig. 1. (a) Crystal structure of the chalcogenide spinels AYb_2X_4 ($A = \text{Cd}$ and Mg , $X = \text{S}$ and Se). While the tetrahedrally coordinated nonmagnetic A sites form a diamond cubic sublattice, the magnetic Yb sites form a pyrochlore lattice with corner-sharing tetrahedra. Temperature dependence of (b) the inverse magnetic susceptibility $1/\chi$ measured under 0.1 T and (c) the total specific heat C_p at 0 T of the chalcogenide spinels AYb_2X_4 .

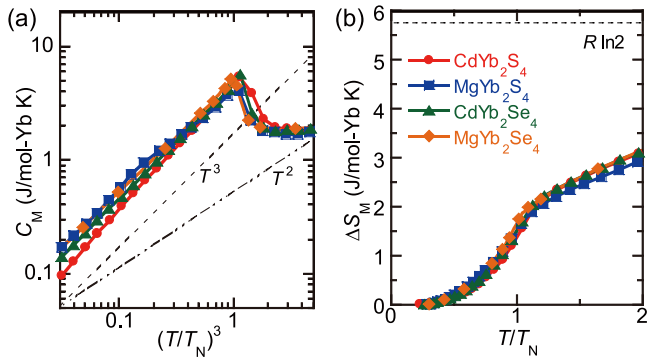


Fig. 2. (a) Full logarithmic plot of the magnetic specific heat C_M vs. $(T/T_N)^3$ of the chalcogenide spinels AYb_2X_4 ($A = \text{Cd}$ and Mg , $X = \text{S}$ and Se). The dashed and two dot-dashed lines indicate the slopes for the T^3 and T^2 laws, respectively. (c) T/T_N dependence of the magnetic entropy ΔS_M of the chalcogenide spinels AYb_2X_4 .

Heisenberg spins has been predicted to host an equally exotic magnetic ground state [3]. As one of the archetypes, $\text{Gd}_2\text{Ti}_2\text{O}_7$ has attracted much attention and extensive studies have revealed frustrated magnetism with unconventional AF ordering [4].

However, other than Gd, most of the rare earth ions in the pyrochlore oxides are known to have a strong trigonal crystal electric field (CEF) that stabilizes either Ising or XY planar local symmetry. To develop a deep understanding of frustrated magnetism in Heisenberg pyrochlore antiferromagnets, we have focused on spinel type AF materials AR_2X_4 , where the rare earth R forms the pyrochlore lattice with different coordination from the oxides and possesses a nearly cubic site symmetry that can lead to Heisenberg spins.

Experimental studies on polycrystalline samples of the Yb-based chalcogenide spinels AYb_2X_4 ($A = \text{Cd}$ and Mg , $X = \text{S}$ and Se) [5] have revealed frustrated quantum magnetism due to antiferromagnetically coupled Heisenberg spins on the pyrochlore lattice [6]. As shown in Fig. 1(a), the AYb_2X_4 families have the spinel structure with the space group $Fd\bar{3}m$. The Yb^{3+} forms the pyrochlore lattice with the six-fold chalcogen X^{2-} coordination and the point symmetry is D_{3d} . The CEF analysis indicates the Yb ground state has nearly Heisenberg spins with a strong quantum character of the ground-state doublet due to the mixing of important components including $\pm J_z = 1/2$. Our low-temperature susceptibility (Fig. 1(b)) and specific heat (Fig. 1(c)) measurements have revealed that all the materials exhibit AF order at $T_N = 1.4 - 1.8$ K, much lower temperatures than the AF exchange coupling scale of ~ 10 K. The magnetic specific heat C_M shows a T^3 dependence, indicating the gapless feature expected for a linearly dispersive Nambu-Goldstone mode in 3D systems [Fig. 2(a)]. Figure 2(b) indicates the temperature dependence of the entropy $\Delta S_M = S_M(T) - S_M(0.4 \text{ K})$. The ΔS_M at T_N is strongly suppressed to $\sim 30\%$ of $R \ln 2$ due to the geometrical frustration. Muon spin rotation/relaxation (μSR) measurements have confirmed the commensurate and incommensurate ordered states in CdYb_2S_4 and MgYb_2S_4 , respectively, and a small local field at the muon site, which indicate the significantly reduced size of the ordered moment in comparison with the bare moment size $1.33 \mu_B/\text{Yb}$, suggesting strong quantum fluctuations in the Yb-based chalcogenide spinels AYb_2X_4 .

References

[1] M. J. Harris *et al.*, Phys. Rev. B **79**, 2554 (1997); A. P. Ramirez *et al.*, Nature **399**, 333 (1999); M. J. P. Gingras and P. A. McClarty, Rep. Prog. Phys. **77**, 056501 (2014).

[2] S. Nakatsuji, Phys. Rev. Lett **96**, 087204 (2006); J. -J. Wen *et al.*, Phys. Rev. Lett. **118**, 107206 (2017).
 [3] R. Moessner and J. T. Chalker., Phys. Rev. Lett. **80**, 2929 (1998).
 [4] N. P. Raju *et al.*, Phys. Rev. B **59**, 14489 (1999); B. Javanparast *et al.*, Phys. Rev. Lett. **114**, 130601 (2015).
 [5] L. Pawlak *et al.*, J. Magn. Magn. Mater. **76-77**, 199 (1988); G. C. Lau *et al.*, Phys. Rev. B **72**, 054411 (2005).
 [6] T. Higo, K. Iritani, M. Halim, W. Higemoto, T. U. Ito, K. Kuga, K. Kimura, and S. Nakatsuji, Phys. Rev. B **95**, 174443 (2017).

Authors

T. Higo, K. Iritani, M. Halim, W. Higemoto^a, T. U. Ito^a, K. Kuga^b, K. Kimura^c, and S. Nakatsuji^a
^aJapan Atomic Energy Agency
^bRIKEN
^cOsaka University

Disordered Route to the Coulomb Quantum Spin Liquid: Random Transverse Fields on Spin Ice in $\text{Pr}_2\text{Zr}_2\text{O}_7$

Nakatsuji Group

As water freezes into ice, ordinal magnets become “solid” (magnetic ordered state), where all the spins are aligned along certain directions, by decreasing temperature. On the other hand, spins are fluctuating like in a liquid state even at very low temperatures in the theoretically predicted exotic state, quantum spin liquid. $\text{Pr}_2\text{Zr}_2\text{O}_7$ is a rare example of such quantum spin liquids, so-called quantum spin ice, where the 2-in 2-out ice rule is partially melted.

The research groups of Prof. Collin Broholm at Johns Hopkins University and Prof. Satoru Nakatsuji at ISSP have been collaborating on the study of the quantum spin ice material $\text{Pr}_2\text{Zr}_2\text{O}_7$. The research team has recently performed the inelastic neutron scattering experiments in $\text{Pr}_2\text{Zr}_2\text{O}_7$ to reveal the origin of the strong quantum fluctuations [1]. The momentum transfer, \mathbf{q} , dependent inelastic pattern at low energy region as shown in Fig.1 (a) indicates the spin ice correlations, which is consistent with the previous work [2]. On the other hand, \mathbf{q} independent pattern appears at high energy region as shown in Fig.1 (c). The latter was found attributable to the splitting of the non-Kramers ground doublet of Pr^{3+} due to the crystal disorder. In fact, all of the

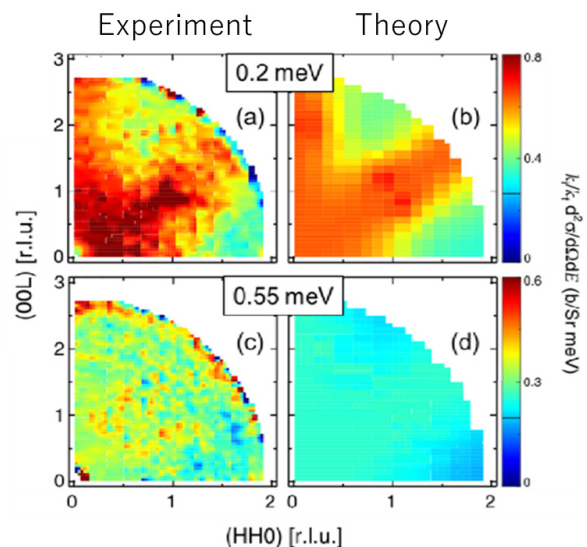


Fig. 1. Inelastic neutron scattering \mathbf{q} map obtained from the experiment at 50 mK for (a) low energy (0.2 meV) region and (c) high energy region (0.55 meV) and the calculation for (b) 0.2 meV and (d) 0.55 meV.

results are well reproduced by the calculation assuming the classical spin ice in the transverse field coming from the structural disorder, which in fact stabilizes the quantum spin ice state.

It has long been known that the crystal disorder disturbs the spin liquid state by forming a spin glass state. This study causes the stir in this wisdom and provides key information to discover new quantum spin liquid materials, which can lead to the future applications such as quantum computer and spintronic devices using the entangled state of quantum spin ice.

References

- [1] J. -J. Wen, S. M. Koohpayeh, K. A. Ross, B. A. Trump, T. M. McQueen, K. Kimura, S. Nakatsuji, Y. Qiu, D. M. Pajerowski, J. R. D. Copley, and C. L. Broholm, *Phys. Rev. Lett.* **118**, 107206 (2017).
 [2] K. Kimura, S. Nakatsuji, J. -J. Wen, C. Broholm, M. B. Stone, E. Nishibori, and H. Sawa, *Nature Communications* **4**, 1934 (2013).

Authors

J. -J. Wen^{a,b}, S. M. Koohpayeh^a, K. A. Ross^{a,c}, B. A. Trump^a, T. M. McQueen^a, K. Kimura^d, S. Nakatsuji, Y. Qiu^c, D. M. Pajerowski^c, J. R. D. Copley^c, and C. L. Broholm^{a,c}
^aThe Johns Hopkins University
^bStanford University
^cNIST Center for Neutron Research, National Institute of Standards and Technology
^dOsaka University

Pressure-Induced Magnetic Transition Exceeding 30 K in the Yb-based Heavy-Fermion β -YbAlB₄

Nakatsuji and Uwatoko Groups

Intermetallic heavy-fermion (HF) compounds, based mostly on Ce, Yb, or U, undergo a quantum phase transition at zero temperature induced by the competition between Kondo effects and intersite magnetic RKKY (Ruderman-Kittel-Kasuya-Yosida) interaction. In these materials, various types of exotic phenomena such as non-Fermi-liquid behaviors and unconventional superconductivity (SC) have been observed near a quantum critical point (QCP). The delicate balance associated with the QCP can be tuned by varying control parameters such as magnetic field, chemical doping, and external pressure. In particular, for the Yb-based HF systems, long-range magnetic order is expected to be stabi-

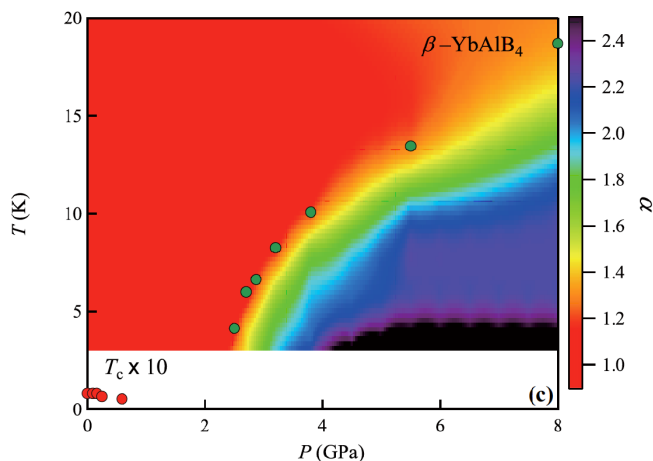


Fig. 1. Pressure-temperature phase diagram for β -YbAlB₄ with a contour plot of the power-law exponent α , which is defined using $\rho = \rho_0 + AT^\alpha$.

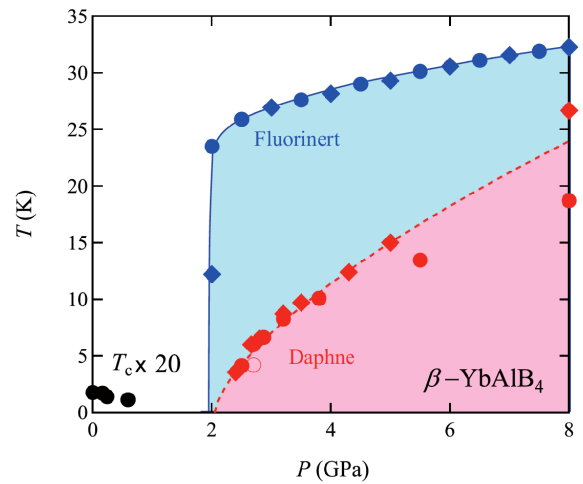


Fig. 2. Pressure-temperature phase diagram for β -YbAlB₄ using two different pressure-transmitting media, Daphne 7373 (red symbols) and Fluorinert (blue symbols), respectively. The phase-transition temperature T_M is determined from the anomalies in the temperature derivative of the resistivities, $d\rho_{ab}/dT$. Solid and open circles mark the transitions determined by the electrical resistance obtained from the cubic-anvil and piston cylinder-type pressure measurements, respectively. The blue solid line is a guide for the eye. The red dashed line is a fit of our data to the function of $(P - P_c)^{2/3}$ expected for a 3D antiferromagnetic ordering.

lized at high pressure. This is because the 4f moments are generally known to become more localized by reducing volume, in sharp contrast to their Ce-based counterparts. For β -YbAlB₄, in which recently observed HF superconductivity at 80 mK and the QCP at zero field at ambient pressure [1-3], of interest is how unconventional quantum criticality observed without tuning, associated with magnetic order that is expected to emerge under high pressure.

Here we report the results of our recent transport study on the HF superconductor YbAlB₄ under pressure [4]. Measurements of the electric resistivity $\rho(T)$ under pressure up to 8 GPa were performed on high-quality single crystals of the Yb-based heavy-fermion system β -YbAlB₄ in the temperature range $2 < T < 300$ K. In the resistivity data, we observed pressure-induced magnetic ordering above the critical pressure $P_c \sim 2$ GPa. (See Fig. 1) Moreover, the clear difference in the phase diagram of Fig. 2 under pressure using two types of pressure media indicates that the transition temperature may be further enhanced under application of uniaxial pressure. With pressure, this phase-transition temperature T_M is enhanced, reaching 32 K at 8 GPa, which is the highest transition temperature so far recorded for the Yb-based heavy-fermion compounds. The power-law exponent α in $\rho = \rho_0 + AT^\alpha$ below T_M gradually changes from $3/2$ to $5/2$ with increasing pressure from 2 to 8 GPa (See Fig. 1). In contrast, the resistivity exhibits a T -linear behavior in the temperature range $2 < T < 20$ K and is insensitive to pressure below P_c . In this pressure regime, the magnetization is also nearly independent of pressure and shows no anomaly above 2 K. Our results indicate that a QCP for β -YbAlB₄ is also located near P_c in addition to the strange metal region near the ambient pressure. While almost pressure independent resistivity and magnetization are observed in the pressure range $0 < P < 2$ GPa, the magnetic phase transition of β -YbAlB₄ was suddenly found at $P > 2$ GPa.

Significantly, the phase transition T_M of β -YbAlB₄ reaches 32 K under 8 GPa and is expected to be further enhanced at higher pressure. Such high magnetic transi-

tion temperatures over 10 K have never been achieved in Yb-based HF materials. Generally, because the *f*-electron moment is sufficiently localized, the magnetic ordering temperatures in HF compounds is often observed below around 10 K. In particular, that of Yb-based HF should be lower than that of Ce-based HF because the Yb *f*-electron is usually more localized than that for Ce.

In previous work for β -YbAlB₄, it is reported that the state showing unconventional critical behavior (the SC phase and ambient-pressure quantum criticality) is separated from this magnetically ordered state by the Fermi-liquid phase [5]. Of high interest is the fact that the non-Fermi-liquid state at ambient pressure robustly persists up to a critical pressure of around 0.4 GPa. Generally, the HF compounds display quantum criticality at the border of magnetism. Thus, these are not features that are expected for magnetically mediated superconductivity. The Yb-based heavy-fermion with non-integer valence may exhibit critical phenomena with not only spin fluctuations but also valence fluctuations at quantum criticality. This valence fluctuation is presumably the key to understanding the origin of the extensive region of the quantum criticality found near ambient pressure and the extremely high ordering temperature of around 30 K found under high pressure.

References

- [1] Y. Matsumoto, S. Nakatsuji, K. Kuga, Y. Karaki, N. Horie, Y. Shimura, T. Sakakibara, A. H. Nevidomskyy, and P. Coleman, *Science* **331**, 316 (2011).
- [2] K. Kuga, Y. Karaki, Y. Matsumoto, Y. Machida, and S. Nakatsuji, *Phys. Rev. Lett.* **101**, 137004 (2008).
- [3] S. Nakatsuji, K. Kuga, Y. Machida, T. Tayama, T. Sakakibara, Y. Karaki, H. Ishimoto, S. Yonezawa, Y. Maeno, E. Pearson *et al.*, *Nat. Phys.* **4**, 603 (2008).
- [4] T. Tomita, K. Kuga, Y. Uwatoko, and S. Nakatsuji, *Phys. Rev. B* **94**, 245130 (2016).
- [5] T. Tomita, K. Kuga, Y. Uwatoko, and S. Nakatsuji, *Science* **394**, 506 (2015).

Authors

T. Tomita, K. Kuga, Y. Uwatoko, and S. Nakatsuji

Orthogonal Magnetization and Symmetry Breaking in Pyrochlore Iridate Eu₂Ir₂O₇

Nakatsuji Group

It has long been known that magnets are magnetized along the external magnetic field. However, magnetization perpendicular to the field is also expected according to thermodynamic theory. This orthogonal magnetization is so tiny that no study so far had been able to detect it experimentally.

Tian Liang and their collaborators in Princeton University and the Massachusetts Institute of Technology in the U.S. and the research group led by Professor Satoru Nakatsuji noticed slight changes in magnetization in the pyrochlore iridate Eu₂Ir₂O₇ following metal-insulator transition accompanied by the all-in all-out magnetic order (Fig 1 (a)). Usually, only the magnetic component parallel to the field is detected when measuring magnetization; the researchers thus attempted to detect magnetization perpendicular to the field by measuring the torque magnetometry, or force producing the tendency of magnets to rotate in a magnetic field, by cantilever and found that orthogonal magnetization abruptly increases below the metal-insulator transition temperature. The group determined that orthogonal magnetization derives

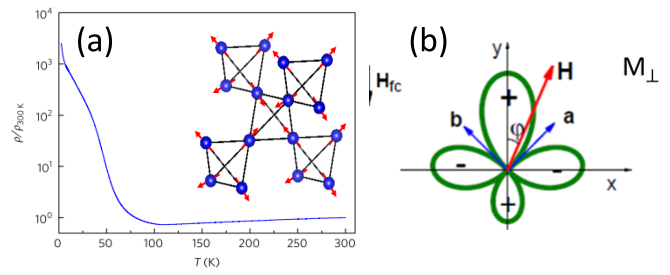


Fig. 1 (a) Metal insulator transition observed in the temperature dependence of the resistivity for Eu₂Ir₂O₇ (main panel) and all-in all-out magnetic order (inset). (b) Octupole moment obtained from the orthogonal magnetization.

from the special spatial distribution of the magnetic charge (magnetic octupole, Fig. 1 (b)), and that this is the origin (order parameter) of the metal-insulator transition.

This tiny orthogonal magnetization is instrumental in initiating the transition of metal into insulator, and carries the potential for use in such applications as magnetic memory and magnetic sensors. This work also gives a hint how to control the transport properties in Pyrochlore iridate, where the mysterious spontaneous anomalous Hall effect in nonmagnetic metallic phase with topological band structure is observed [2].

References

- [1] T. Liang, T. H. Hsieh, J. J. Ishikawa, S. Nakatsuji, L. Fu, and N. P. Ong, *Nature Physic* **13**, 599 (2017)
- [2] Y. Machida, S. Nakatsuji, S. Onoda, T. Tayama, and T. Sakakibara, *Nature* **463**, 210 (2010).

Authors

T. Liang^a, T. H. Hsieh^b, J. J. Ishikawa, S. Nakatsuji, L. Fu^b, and N. P. Ong^a

^aPrinceton University

^bMassachusetts Institute of Technology

Helical Magnetism in the Vicinity of the Superconducting State in MnP

Uwatoko, Kato, and Sugino Groups

MnP exhibits superconductivity under pressure with a maximum transition temperature of ~1 K at 8 GPa [1]. Since Mn has the spin degree of freedom, elucidating the magnetic contribution to the superconductivity is crucial to understand the pairing mechanism. In particular, the magnetic state in the vicinity of the superconducting phase needed to be clarified. In order to study the pressure dependence of the magnetic ground state in MnP, high pressure neutron diffraction measurements were performed up to 3.8 GPa [2]. The high pressures below and above 2 GPa were generated with a self-clamped piston-cylinder cell and a palm cubic anvil cell, respectively.

MnP shows a ferromagnetic order below $T_c \sim 290$ K followed by a helical order (helical-*c*, Fig. 1a) with the spins lying in the *ab* plane and the helical rotation propagating along the *c* axis below $T_s \sim 50$ K at ambient pressure [3,4]. With increasing pressure, we found that both T_c and T_s are gradually suppressed and the helical order disappears at ~1.2 GPa. At intermediate pressures of 1.8 and 2.0 GPa, the ferromagnetic order first develops and then is suppressed at a lower temperature (T^*). New incommensurate magnetic peaks split along the *b* axis appear below T^* . The new

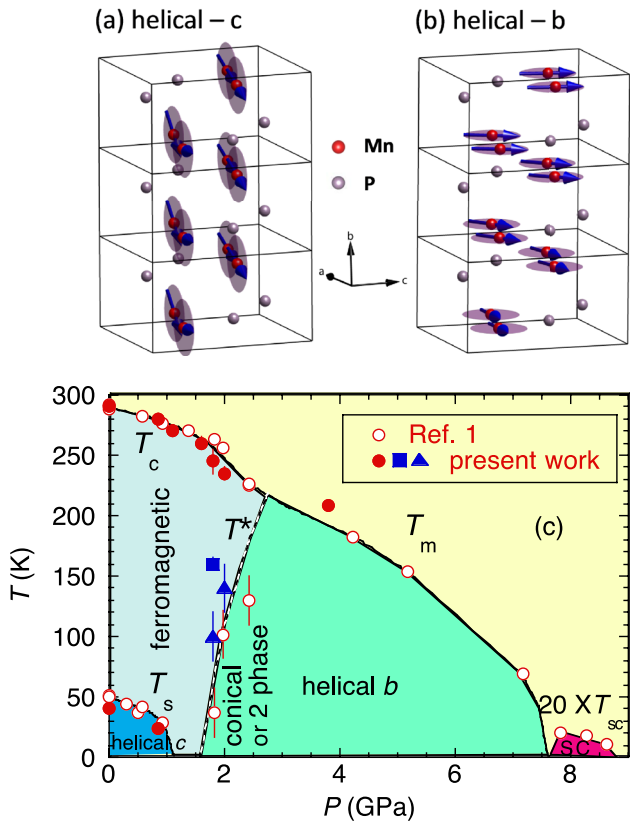


Fig. 1. Helical spin structures under low (helical-c) (a) and high pressures (helical-b) (b). (c) Temperature-pressure phase diagram. The open and filled symbols represent the data in Ref. 1 and the present results, respectively. The filled square is the temperature where the incommensurate magnetic peaks start to develop. The filled triangles are the temperatures where the commensurate magnetic signal starts to decrease.

magnetic peaks originate from another helical structure, which hosts the spins in the ac plane and the propagation along the b axis (helical- b , Fig. 1b). Since the ferromagnetic component still remains, the magnetic ground state is a conical or two-phase (ferromagnetic and helical- b) structure. Above 2 GPa, a magnetic transition from paramagnetic directly to the helical- b states appears below T_m . The magnetic phase diagram is shown in Fig. 1c. The magnetic state close to the superconducting phase was found to be the helical- b structure.

In the helical- b phase, the helical transition temperature and the ordered moment decrease with increasing pressure. On the other hand, the magnetic incommensurability becomes larger with increasing pressure, indicating that antiferromagnetic interactions become more dominant than ferromagnetic ones, which are influential at low pressures. This suggests that antiferromagnetic fluctuations might be connected to the superconducting pairing mechanism in MnP.

At ambient pressure, MnP is considered to be a localized d electron spin system of Mn, interacting with itinerant s electrons of P, which is reproduced by the s - d model. Applying pressure causes more enhanced orbital overlap between Mn atoms, which gives rise to more itinerancy. The density-functional theory (DFT) calculation shows that the pressure gradually reduces the Mn moments and finally leads to a nonmagnetic state [5]. The Mn moment estimated at 3.8 GPa and 5 K is $0.84(14)\mu_B$, which suggests that the lattice compression is very close to the critical regime where the large d - d overlapping makes the system more itinerant and the spontaneous magnetization does not occur [5]. In Ref. 5, only collinear spin structures (one ferromagnetic and three

antiferromagnetic structures) are considered as potential ground states. The ferromagnetic structure was found to be most stable in MnP until the magnetic moment disappears with compression. This result does not exclude the possibility of a noncollinear magnetic state between ferromagnetic and itinerant nonmagnetic states. Further theoretical studies on the magnetic state in the vicinity of the itinerant nonmagnetic state are desirable.

References

- [1] J.-G. Cheng, K. Matsubayashi, W. Wu, J. P. Sun, F. K. Lin, J. L. Luo, and Y. Uwatoko, Phys. Rev. Lett. **114**, 117001 (2015).
- [2] M. Matsuda, F. Ye, S. E. Dissanayake, J.-G. Cheng, S. Chi, J. Ma, H. D. Zhou, J.-Q. Yan, S. Kasamatsu, O. Sugino, T. Kato, K. Matsubayashi, T. Okada, and Y. Uwatoko, Phys. Rev. B **93**, 100405(R) (2016).
- [3] G. P. Feicher, J. App. Phys. **37**, 1056 (1966).
- [4] J. B. Forsyth, S. J. Pickart, and P. J. Brown, Proc. Phys. Soc. **88**, 222 (1966).
- [5] Z. Gercsi and K. G. Sandeman, Phys. Rev. B **81**, 224426 (2010).

Authors

M. Matsuda^a, F. Ye^a, S. E. Dissanayake^a, J.-G. Cheng^b, S. Chi^a, J. Ma^c, H. D. Zhou^c, J.-Q. Yan^{a,c}, S. Kasamatsu, O. Sugino, T. Kato, K. Matsubayashi, T. Okada, and Y. Uwatoko
^aOak Ridge National laboratory
^bBeijing National Laboratory for Condensed Matter Physics and Institute of Physics, Chinese Academy of Sciences
^cUniversity of Tennessee, Knoxville

Mechanism of High-Temperature Superconductivity in FeSe Unveiled via the Magneto-Transport Measurements under High Pressures

Uwatoko and Yamashita Groups

Recently, the layered β -FeSe has aroused tremendous research interest due to the observations of many intriguing physical properties. At ambient pressure, FeSe develops an electronic nematicity below $T_s = 90$ K, which, however, is not accompanied by any long-range magnetic order. The absence of static magnetism in FeSe is in strikingly contrast with the majority of parent compounds of FeAs-based superconductors. Interestingly, it was found that a static magnetic order emerges at pressures above 1 GPa and the transition temperature T_m increase concomitantly with the

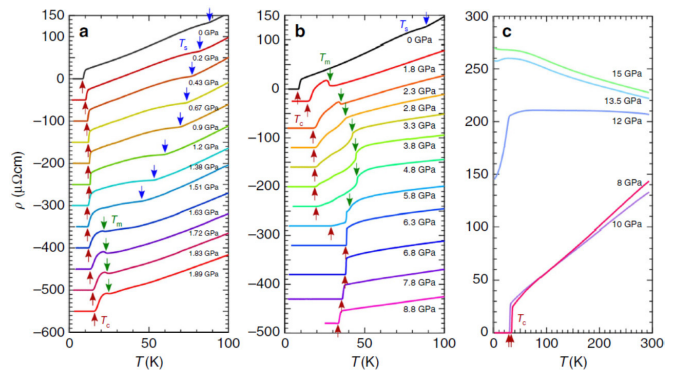


Fig. 1. Temperature dependence of resistivity $\rho(T)$ in FeSe single crystals under high pressure. (a) $\rho(T)$ curves below 100 K at different pressures up to 1.9 GPa measured in the PCC. (b) $\rho(T)$ up to 8.8 GPa measured with the CAC. (c) $\rho(T)$ up to 15 GPa measured with a smaller CAC. Except for (c) the $\rho(T)$ curves are vertically shifted for clarity. The resistive anomalies at transition temperatures T_s , T_m , and T_c are indicated by the arrows.

superconducting transition temperature T_c up to 2.5 GPa. The relatively low $T_c \approx 9$ K of FeSe at ambient pressure can be enhanced significantly to $T_c^{\max} \sim 40$ K at about 7 GPa, however, the evolution of $T_m(P)$ and its relationship with T_c remains largely unknown for $P > 2.5$ GPa due to the constraints of high-pressure techniques.

Thus, a comprehensive T-P phase diagram of FeSe is highly desirable in order to achieve a better understanding on the interplay of high- T_c superconductivity with magnetism and/or nematicity, which is commonly believed as an essential issue for the iron-based superconductors. For this purpose, we have carried out a detailed magneto-transport study on the FeSe single crystals up to 15 GPa by using the piston-cylinder cell (PCC) and the cubic-anvil-cell (CAC) apparatus; the latter has the merits of good hydrostaticity and large pressure capability.

Figure 1(a) displays the temperature dependence of resistivity $\rho(T)$ for FeSe single crystal under pressures up to 1.9 GPa measured with PCC. We can see clearly that the nematic order at T_s manifested as an upturn in $\rho(T)$ is suppressed gradually by pressure and smears out above 1.5 GPa. Nearly at the same pressure, another upturn anomaly appears at $T_m = 20$ K corresponding to the emergence of static magnetic order, and T_m increases gradually with pressure. In this pressure range, T_c defined as the zero-resistivity temperature first increases, and then decreases slightly before raising again. $\rho(T)$ data shown in Fig. 1(b) measured with CAC can further track the evolutions of T_c and T_m . As can be seen, T_m increases gradually with pressure, but the upturn anomaly becomes weaker, and changes to a downward anomaly at 2.8 GPa. T_m reaches the maximum of 45 K at ~ 5 GPa, above which T_m disappears quickly and merges with T_c . Within the pressure range where T_m increases, T_c keeps nearly unchanged at ~ 20 K, and then the suppression of T_m is accompanied with a sudden enhancement of T_c . The maximum T_c of 38.3 K is achieved at 6.3 GPa where the magnetic order just collapses. Above 6.3 GPa, T_c decreases slowly with pressure until ~ 12 GPa, above which FeSe adopts a three-dimensional NiAs-type structure and becomes semiconducting.

We have further performed measurements of $\rho(T)$ under various magnetic fields for each pressure. The insensitivity of T_m to external magnetic field rules out the possible cause of resistivity drop at T_m due to the onset of superconductivity. In addition, we also measured the ac magnetic susceptibility $\chi(T)$ up to 8.8 GPa to determine T_c and obtained nearly

consistent results with resistivity.

Based on these above results, we constructed the most comprehensive T-P phase diagram of FeSe as shown in Fig. 2, from which we can see explicitly how the three competing orders evolve under pressure. The application of high-pressure destabilizes the nematic order and then induces the long-range magnetic order, confirming the competing nature of these two electronic orders. When T_s is completely suppressed around 2 GPa, T_c experiences the first step increase to ~ 20 K. But T_c keeps nearly constant when T_m increases with pressure, which demonstrates the competing nature of magnetic order with superconductivity. The magnetic order is finally destabilized upon further increasing pressure to around 6 GPa when T_c undergoes a sudden jump to ~ 40 K.

For the first time, we uncover the dome shape of magnetic phase superseding the nematic order, and demonstrate that the high- T_c superconductivity in FeSe is achieved by suppressing the long-range magnetic order. This is quite similar with the situations seen in the FeAs-based superconductors. To achieve a better understanding on the importance of magnetic fluctuations, further studies on the electronic structure of FeSe under high pressures are needed. It is also interesting to note that the obtained phase diagram highlights unique features of FeSe among the iron-based superconductors, but bears some resemblance to that of high- T_c cuprates.

Reference

Sun J. P. *et al.*, Nat. Commun. 7, 12146 (2016).

Authors

J.P. Sun^a, K. Matsuura^b, G. Z. Ye^{a,c}, Y. Mizukami^b, M. Shimozawa, K. Matsubayashi^d, M. Yamashita, T. Watashige^e, S. Kasahara^c, Y. Matsuda^c, J.-Q. Yan^{f,g}, B.C. Sales^e, Y. Uwatoko, J.-G. Cheng^a, and T. Shibauchi^b

^aNational Laboratory for Condensed Matter Physics and Institute of Physics, Chinese Academy of Sciences

^bUniversity of Tokyo

^cSchool of Physical Science and Technology, Yunnan University

^dThe University of Electro-Communications

^eKyoto University

^fMaterials Science and Technology Division, Oak Ridge National Laboratory

^gUniversity of Tennessee

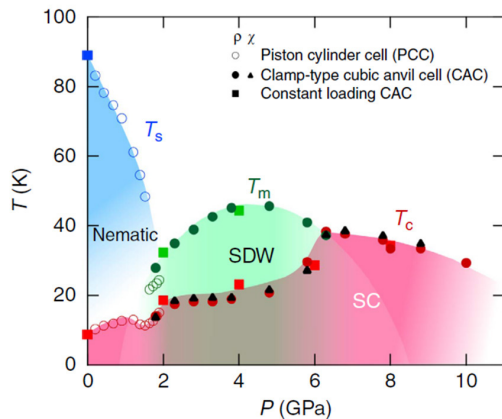


Fig. 2. T-P phase diagram of bulk FeSe. The structural (T_s , blue), magnetic (T_m , green), and superconducting transition temperatures (T_c , red and black) as a function of hydrostatic pressure in high-quality single crystals are determined by anomalies in resistivity $\rho(T)$ and ac magnetic susceptibility $\chi(T)$ measured in the PCC and CAC.

Absence of Superconductivity in the Collapsed Tetragonal Phase of KFe_2As_2 under Hydrostatic Pressures

Uwatoko Group

High pressure phase diagram of the tetragonal KFe_2As_2 remains controversial because of the strong sensitivity of superconducting transition temperature (T_c) depending on the type of the pressure cells and the pressure transmitting medium. Specially, the superconductivity of the collapsed tetragonal KFe_2As_2 is an open question since there are no zero resistivity state in the previous studies [1-3], presumably due to the pressure inhomogeneity or the non-hydrostaticity. To resolve these issues pertaining to this intriguing compound, we studied the temperature dependence of resistivity on KFe_2As_2 single crystals down to 20 mK under various much improved hydrostatic pressures up to 17.5 GPa generated in a cubic anvil cell.

Figure 1 shows the superconducting phase diagram and the superconducting transition widths of KFe_2As_2 under pressure with the previous data for comparison.

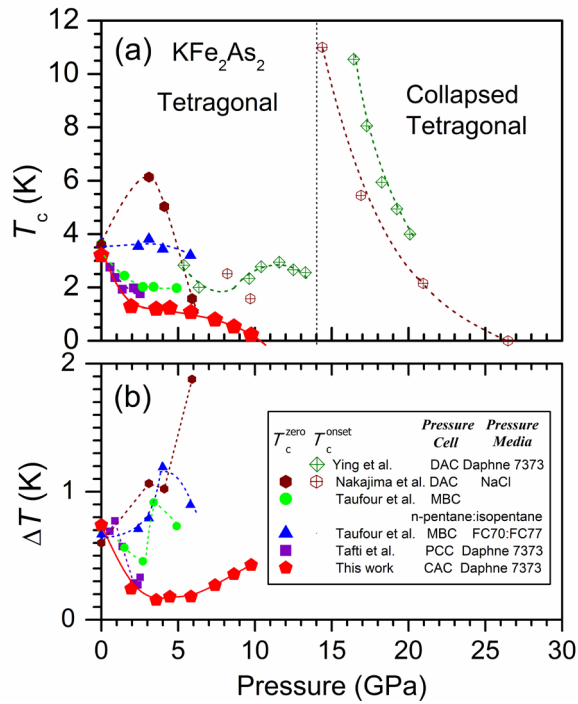


Fig. 1. (a) Temperature-Pressure phase diagram of KFe_2As_2 . The solid and open symbols represent the zero resistivity state temperature T_c^{zero} and the onset temperature T_c^{onset} of superconducting transition, respectively. (b) $\Delta T_c (= T_c^{\text{onset}} - T_c^{\text{zero}})$ as a function of pressure. “DAC”, “MBC”, “PCC”, “CAC” represent diamond anvil cell, modified Bridgeman method, piston cylinder cell, and cubic anvil cell, respectively.

Pressure dependence of T_c has several distinct features: firstly, superconducting transition width ΔT_c becomes much narrower in the same pressure region. As the pressure increases, ΔT_c decreases and is ~ 0.2 K for $1.9 < P < 5.8$ GPa; and zero resistivity state retains up to 11 GPa where the superconducting state disappears. While in other reports, the superconducting transition becomes broad evidently as the pressure increases and ΔT increases to ~ 0.5 -2 K depending on the pressure apparatus; zero resistivity state cannot be achieved above 7 GPa. Secondly, T_c obtained is lower than others in the same pressure regions in Fig. 1(a). As proposed, T_c of tetragonal KFe_2As_2 depends sensitively on pressure conditions and was enhanced if under a less hydrostatic condition [3]. These characteristic suggests a much improved hydrostatic pressure condition in a cubic anvil cell in comparison with the piston cylinder cell (PCC) or diamond anvil cell (DAC) under higher pressure. We examined the resistivity of KFe_2As_2 in the pressure region of $14 < P < 17.5$ GPa, however, superconductivity does not appear down to 2 K, which are contrary to the previous results using DAC [1,2]. In striking contrast to previous reports in Fig. 1, no superconducting phase emerges upon further increasing pressures until the collapsed tetragonal KFe_2As_2 forms and it was argued that such a discrepancy can be attributed to the different pressure apparatus or homogeneity.

We studied the temperature dependence of resistivity $\rho(T)$ under pressures by adopting an empirical formula $\rho = \rho_0 + A_1T + A_2T^2$ to construct a qualitative relation between the evolution of temperature coefficient and the T_c . Here, the T^2 term is to describe the Fermi liquid state and the T -linear term is associated with the electronic correlations and scattering process such as the electron-boson interaction and/or critical fluctuations near QCP. The parameters were presented Fig. 2. The residual resistivity ρ_0 decreases monotonically, and starts to increase at 14 GPa, then jumps to nearly three times with the pressure increasing

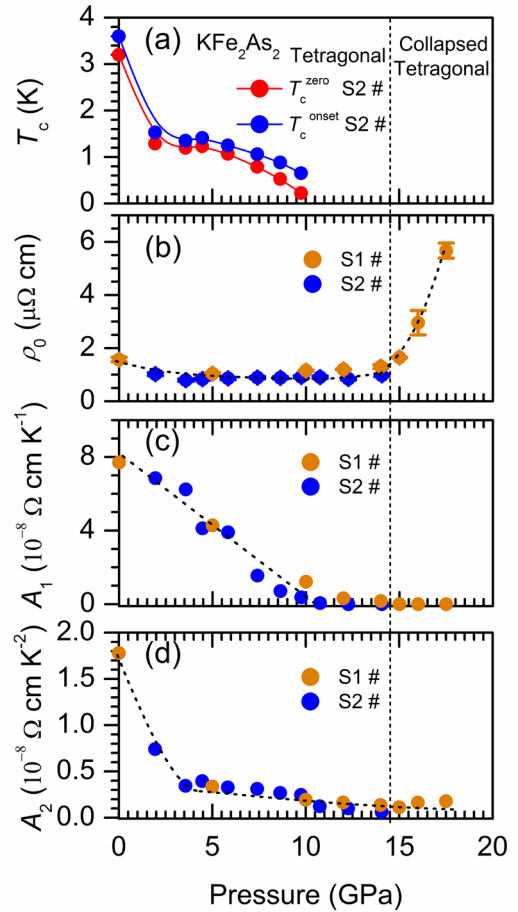


Fig. 2. The evolutions of parameters under pressure: (a) T_c^{onset} and T_c^{zero} ; (b) ρ_0 ; (c) A_1 ; (d) A_2 . The dashed line indicated phase transformation at lower temperature.

up to 17.5 GPa, which is sharply different from the reports by using DAC [1]. As the pressure increases, A_1 decreases linearly and becomes almost zero around 11 GPa, coinciding with the suppression of T_c . This close connection between T_c and A_1 suggests that the scattering mechanism leading to the T -linear term play an important role for the appearance of SC in KFe_2As_2 . On the other hand, A_2 decreases rapidly with approaching P_{c1} , and then gradually decreases with further increasing pressure. Furthermore, this observation is in agreement with a magnetic quantum critical point located at a negative pressure [4]. Incidentally, the shallow minimum of T_c near ~ 2 GPa is not explicable in terms of the pressure dependence of A_1 and A_2 . Other factors such as pressure variation of the density of state at the Fermi level, balance between intra- and inter-Fermi-surface-pockets scattering affect T_c . The combined interplays of those factors would be important to fully understand the evolution of T_c under pressure.

References

- [1] Y. Nakajima, *et al.*, Phys. Rev. B. **91**, 060508 (R) (2015).
- [2] J. J. Ying *et al.*, arXiv: 1501.00330 (2015).
- [3] V. Taufour, *et al.*, Phys. Rev. B **89**, 220509(R) (2014).
- [4] P. S. Wang, *et al.*, Phys. Rev. B. **93**, 085129 (2016).

Authors

B. Wang, K. Matsubayashi, J. Cheng^a, T. Terashima^b, K. Kihou^c, S. Ishida^c, C.-H. Lee^c, A. Iyo^c, H. Eisaki, and Y. Uwatoko^a
^aBeijing National Laboratory for Condensed Matter Physics and Institute of Physics, CAS
^bNational Institutes for Materials Science
^cNational Institute of Advanced Industrial Science and Technology (AIST)

Morphology of High-Genus Fluid Vesicles

Noguchi Group

The nucleus of a eukaryotic cell is surrounded by a nuclear envelope. The nuclear envelope consists of two bilayer membranes connected by many lipidic pores, which are supported by a protein complex called nuclear pore complex (NPC). Nuclear pores have an approximately uniform distribution in the nuclear envelope. Hence, the nuclear envelope is a spherical stomatocyte with a high genus. In order to clarify the formation mechanism of the nuclear envelope, we simulated the morphology of high-genus vesicles by dynamically triangulated membrane methods.

First, we investigated the vesicle morphology of genus $0 \leq g \leq 8$ in the absence of NPCs (see Fig. 1(a)–(f)) [1]. For $g \geq 3$, bending-energy minimization without volume or other constraints produces a circular-cage stomatocyte, where the pores are aligned in a circular line on an oblate bud (see Fig. 1(a)). As osmotic pressure is imposed to reduce the vesicle (perinuclear) volume, the vesicle transforms to the spherical stomatocyte (nuclear envelope shape) (see Fig. 1(d)). In the lipid vesicles, the area difference ΔA of two monolayers of the bilayer is different from the preferred value ΔA_0 determined by the lipid number of both monolayers. This effect is taken into account by the area-difference elasticity (ADE) energy: $K_{\text{ade}}(\Delta A - \Delta A_0)^2/2$. With increasing ΔA_0 , the vesicle transforms from the circular-cage stomatocyte into discocyte continuously via pore opening (see Fig. 1(b)) at the large volume as seen in genus-0 vesicles. Surprisingly, however, at the small volume, the vesicle exhibits a discrete transition from polyhedron to discocyte (see Figs. 1(e) and (f)). Thus, the pore arrangements change the character of shape transitions.

Next, we modeled the pore size constraint by the NPC as a ring which the membrane cannot penetrate [2]. When the pore is restricted as a small size, the aligned pores move to the end of the vesicle under the bending-energy minimization as shown in Fig. 1(g).

Interestingly, the pore-constraint itself rather presents the formation of the spherical stomatocyte. We found that the spherical stomatocyte is formed by a small perinuclear

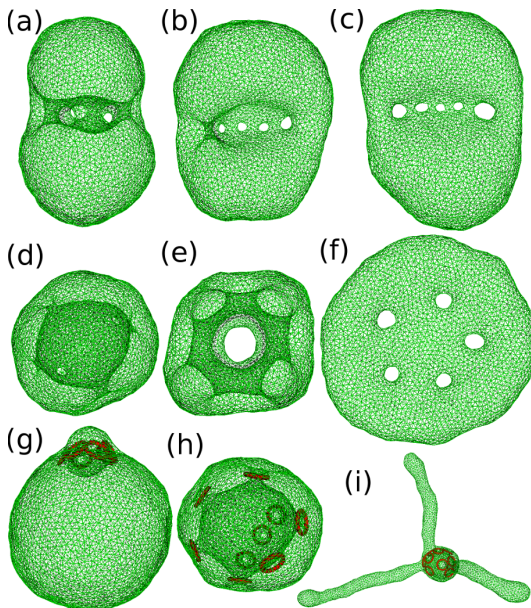


Fig. 1. Snapshots of high-genus vesicles (a–f) with no pore-size constraint and (g–h) with pore-size constraint. (a–g) $g = 5$. (h,i) $g = 8$.

volume, osmotic pressure within nucleoplasm, and/or repulsion between the pores (see Fig. 1(h)). We consider the osmotic pressure by nucleosomes and nuclear proteins in nucleoplasm is the main source to stabilize the nuclear shape. When the ADE energy is accounted, the endoplasmic-reticulum-like tubules can grow from the spherical stomatocyte (see Fig. 1(i)).

References

- [1] H. Noguchi, EPL **112**, 58004 (2015).
- [2] H. Noguchi, Biophys. J. **111**, 824 (2016).

Author

H. Noguchi

Dynamics of Hydrogen Atoms in Nanocrystalline Palladium Hydride

Yamamuro Group

Palladium hydride (PdH_x) is the most popular metal hydride which has been investigated by many physicists and chemists. It has been remarked also from industrial points of view, *e.g.*, hydrogen storage, filters, sensors, catalysts, etc. The physical and chemical properties of nanometer-sized materials have also been actively studied since they are often different from bulk properties owing to their size and/or surface effects. We have performed calorimetric [1] and neutron diffraction [2] studies on nanocrystalline PdH_x and PdD_x . In bulk samples, H atoms are located at the octahedral (O) sites in an fcc lattice (see the inset of Fig. 1). We found that H atoms occupy not only the O sites but also the tetrahedral (T) sites in the subsurface region of nanoparticles.

Recently, we conducted the quasielastic neutron scattering (QENS) and inelastic neutron scattering (INS) works on bulk and nanocrystalline PdH_x [3,4]. These neutron scattering methods are very powerful to explore the dynamics of hydrogen atoms owing to a large incoherent scattering cross section for a H atom. The QENS experiments were performed on HFBS, DCS and NSE at NCNR, NIST (USA) and TOFTOF at FRM II, TUM (Germany), and the INS experiment on 4SEASONS at MLF, J-PARC (Japan).

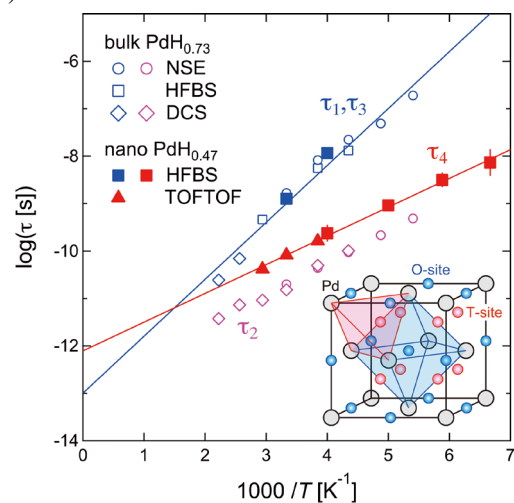


Fig. 1. Arrhenius plots of the relaxation times for the hydrogen motions in nanocrystalline $\text{PdH}_{0.47}$ and bulk $\text{PdH}_{0.73}$. All of the plotted data are the values at $Q = 0.8 \text{ \AA}^{-1}$. The solid lines represent the results of the fits assuming the Arrhenius law. The inset shows the locations of interstitial hydrogen atoms in an fcc Pd lattice; octahedral (O) sites ($1/2, 1/2, 1/2$) and tetrahedral (T) sites ($1/4, 1/4, 1/4$).

Novel Quantum State in a Breathing Pyrochlore Antiferromagnet

Masuda Group

In geometrically frustrated magnet, a macroscopic degeneracy remains even at zero temperature as long as the geometry is preserved. Such a situation contradicts the third law of thermodynamics and small perturbations, which can induce non-trivial quantum states, play an important role in avoiding the breakdown of the basic law. A classic example of the violation of the third law is given by a regular tetrahedron of $S = 1/2$ Heisenberg spins; this has a nonmagnetic ground state with a two-fold degeneracy. In nature, however, neither perfect isolation nor absence of coupling to other degrees of freedom is achieved and a non-degenerate state is induced by a perturbation. The search for a simple and isolated system is a challenge to the third law, leading to discovery of new state of matter at very low temperatures. $\text{Ba}_3\text{Yb}_2\text{Zn}_5\text{O}_{11}$ is a rare experimental realization of non-distorted regular tetrahedron spin system as shown in Fig. 1. Magnetic Yb^{3+} ions form breathing pyrochlore lattice, and no phase transition was reported at $T > 0.38$ K [1]. Crystal field excitation measured by using HRC spectrometer in the energy range of $\hbar\omega < 150$ meV exhibited that the Yb^{3+} ion is regarded as an effective spin $S = 1/2$ with small easy-plane anisotropy [2]. We, then, study low energy excitations to identify the ground state of the spin tetrahedra in the real world [3].

The INS spectrum at the base temperature in Fig. 2(a) shows four flat peaks; the excitations are sharp and the system is regarded as isolated. The spectrum is reproduced by the spin tetrahedron model with $J_x = -0.57$ meV, $J_z = -0.56$ meV, $J_{\text{DM}} = 0.11$ meV as shown in Fig. 2(b), and the system includes large Dzyaloshinskii-Moriya (DM) interaction. The DM interaction hybridizes the ground state with the excited ones, leading to the change of selection rule of INS spectrum, but it does not lift the two-fold degeneracy of the ground state in the isolated spin tetrahedron. To observe the real ground state, we measured heat capacity down to very low temperature and estimated the change of the entropy. As shown in Fig. 2(c) the entropy gradually decreases with the temperature and reaches almost zero,

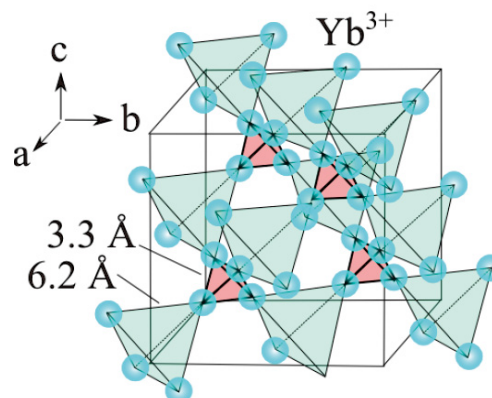


Fig. 1. Crystal structure of $\text{Ba}_3\text{Yb}_2\text{Zn}_5\text{O}_{11}$. Regular tetrahedra of Yb^{3+} ions form breathing pyrochlore lattice.

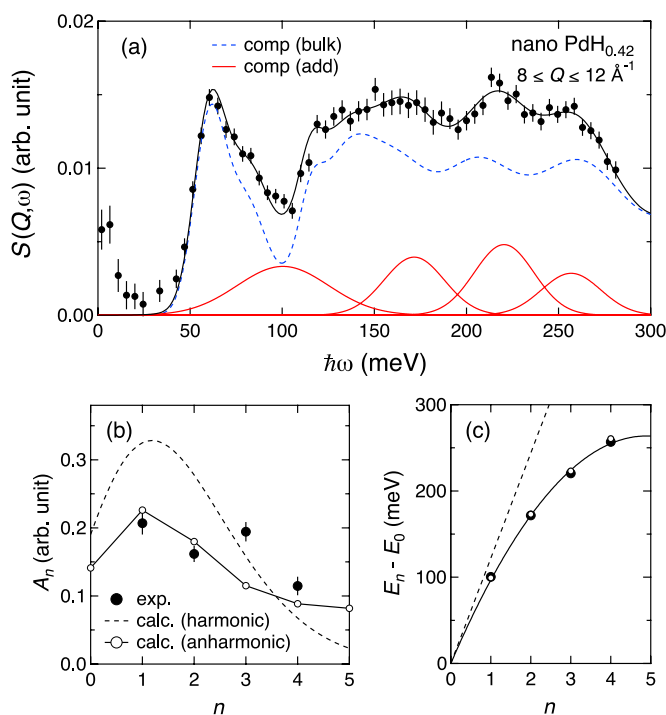


Fig. 2. (a) Inelastic neutron scattering spectrum for nanocrystalline $\text{PdH}_{0.42}$ at 10 K. (b) Intensity and (c) excitation energy against a quantum number n .

Figure 1 shows the temperature dependence of the relaxation times of the hydrogen motions in bulk and nanocrystalline PdH_x [3]. These values were obtained by fitting the QENS spectra to Lorentz functions (τ is an inverse of half width at half maximum) or exponential functions (for NSE data). In the bulk sample, τ_1 and τ_2 are associated with the O-O jump motions among the ground states and among the first excited states, respectively. In the nanocrystalline sample, τ_3 , which is comparable with τ_1 , may be due to the O-O jumps in the interior region of the nanocrystals. On the other hand, τ_4 , which is a novel relaxation, may be due to the T-T jumps at around the subsurface of the nanocrystals taking the previous structural information [2] into consideration.

Figure 2(a) presents the INS spectrum of nanocrystalline $\text{PdH}_{0.42}$ [4]. The spectrum was fitted with the combination of the spectrum of the bulk $\text{PdH}_{0.73}$ (dashed curve) and the additional excitations (solid curves). The additional component was represented by multiple Gaussians taking peak positions, intensities and widths as fitting parameters. The estimated intensities and averaged excitation energies are displayed in Fig. 2(b) and (c). Dashed curves represent the expectation from the quantum harmonic oscillator model (QHO) with $\hbar\nu_0 = 122$ meV. Obviously, the QHO model does not reproduce the experimental results; the data were roughly reproduced by a highly anharmonic trumpet-like potential. The additional excitations are attributed to the H vibrations at the T sites in the subsurface region. Thus, by using neutron scattering techniques, we have obtained structural, diffusion, and vibrational data which are consistent with each other.

References

- [1] H. Akiba *et al.*, Phys Rev. B **92**, 064202 (2015).
- [2] H. Akiba *et al.*, J. Am. Chem. Soc. **138**, 10238 (2016).
- [3] M. Kofu *et al.*, Phys Rev. B **94**, 064303 (2016).
- [4] M. Kofu *et al.*, submitted to Phys Rev. B.

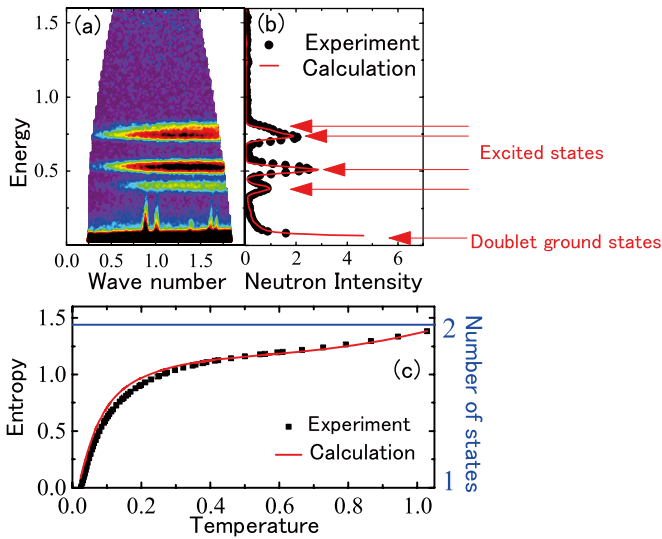


Fig. 2. Neutron spectrum and entropy change of $\text{Ba}_3\text{Yb}_2\text{Zn}_5\text{O}_{11}$. (a) Spectrum measured at 1.5 K. (b) Neutron intensity of the experiment and that of the calculation of the spin tetrahedron model (see the text in detail). (c) Entropy change. Selection of the ground state is observed.

meaning that a unique ground state is selected. Nature, thus, realizes a novel spin liquid state through a perturbative term. As a candidate state, a spin liquid having partial dimer order or chiral order is theoretically predicted in weakly coupled spin tetrahedra. For the further understanding ultra-high-resolution INS experiment at ultra-low temperature is important.

References

- [1] K. Kimura *et al.*, Phys. Rev. B **90**, 060414(R) (2014).
- [2] T. Haku *et al.*, J. Phys. Soc. Jpn. **85**, 034721 (2016). The spectra of the crystal electric field is described in the section of the progress of neutron facility in this activity report.
- [3] T. Haku *et al.*, Phys. Rev. B **93**, 220407(R) (2016). The INS experiment was performed at PELICAN spectrometer installed in ANSTO. The travel expenses for the experiment were supported by General User Program for Neutron Scattering Experiments, Institute for Solid State Physics, the University of Tokyo (proposal No. 15543).

Authors

T. Haku, K. Kimura^a, Y. Matsumoto, M. Soda, M. Sera^a, D. Yu^b, R. A. Mole^b, T. Takeuchi^a, S. Nakatsuji, Y. Kono, T. Sakakibara, L.-J. Chang^c, and T. Masuda

^aOsaka University

^bAustralian Nuclear Science and Technology Organization

^cNational Cheng Kung University

Unveiled Multiferroic Properties in BiFeO_3

Tokunaga Group

Recent extensive studies on multiferroic materials were motivated not only by the interest in basic science, but also by their possible application to magnetic memory devices writable by electric fields with low power consumption. Among various multiferroic materials, BiFeO_3 is perhaps the most extensively studied because of its huge spontaneous electric polarization (P_S) as well as high ordering temperatures. Our recent careful studies of magnetoelectric effects revealed existence of novel electric polarization (P_T) normal to the P_S that can be controlled by magnetic fields in a non-volatile way [1].

The novel P_T is found to couple with magnetic domains of the cycloidal spin order (Q -domains). Owing to the C_3 symmetry of the crystal, there are three equivalent directions

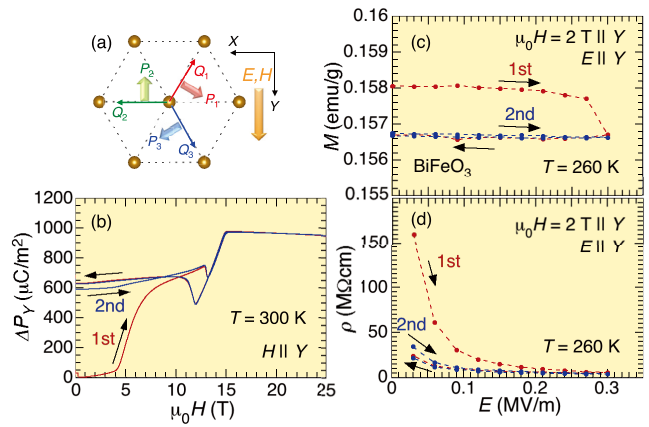


Fig. 1(a) Schematics of BiFeO_3 within the ab -plane. Brown circles represent Fe ions. Thin and thick arrows show propagation vectors of the cycloidal spin order and transverse electric polarization, respectively. (b) Magnetic field dependence of electric polarization measured at 300 K for first and second field cycles. The prominent hysteresis below 10 T in the first field scan corresponds to the reorientation of the magnetoelectric domains. Electric field dependence of (c) magnetization and (d) resistance of BiFeO_3 in the first and second field cycles.

for the spin modulation vector. Thereby, the Q -domains are specified by the vectors Q_1 , Q_2 , and Q_3 shown in Fig. 1(a). Here, each Q -domain contains P_T normal to its Q -vector as illustrated in Fig. 1(a) as P_1 , P_2 , and P_3 . Application of high magnetic field can realize the single Q -domain state. The reorientation process appears as an irreversible change in the electric polarization below 10 T in the first magnetic field cycle as shown in Fig. 1(b).

As a counter effect of this phenomenon, we can expect control of the Q -domains by external electric fields. Such electric control of Q -domains is resolved through magnetization measurements as a function of electric field. In the reorientation process of the Q -domain in the first electric field scan, we observed irreversible change in magnetization as shown in Fig. 1(a) [2]. Simultaneous measurement of the resistance also shows irreversible change only in the first field scan: the resistance at a certain electric field becomes small after application of $E = +0.3$ MV/m [Fig. 1(b)]. Interestingly, this low resistance state can be switched back to the high resistance one by applying $E = -0.3$ MV/m. This switching between high and low resistance states, in other words the bipolar RRAM effects, appears repeatedly at least 20,000 cycles at room temperature [2].

These experimental results revealed the unveiled multiferroic properties in BiFeO_3 will be useful for non-volatile memory devices writable by electric fields, readable simply by measuring their resistance, and stable against external fields at least up to 4 T.

References

- [1] M. Tokunaga *et al.*, Nat. Commun. **6**, 5878 (2015).
- [2] S. Kawachi *et al.*, Appl. Phys. Lett. **108**, 162903 (2016).

Authors

S. Kawachi, H. Kuroe^a, T. Ito^b, A. Miyake, and M. Tokunaga

^aSophia University

^bNational Institute of Advanced Industrial Science and Technology (AIST)

Metamagnetism in the Kondo Insulator YbB_{12} at Ultrahigh Magnetic Fields of up to 120 T

Y. Matsuda and Kindo Groups

Kondo insulator is a fascinating group of materials. When strong interactions between magnetic ions and itinerant band electrons exist, the metallic ground state with heavy mass of the quasi particle may appear. However, in reality, a limited number of materials exhibit insulating ground state due to yet-to-be-defined reason and are termed Kondo insulators. The energy gap opens at a low temperature and simultaneously the magnetic moments are screened most probably due to the Kondo effect. The resultant ground state of the Kondo insulator is non-magnetic insulating state. One may naturally think that the Kondo effect would be suppressed by a high enough magnetic field. Hence, high-magnetic-field experiments on the Kondo insulator is intriguing; the electronic and magnetic properties are expected to change significantly by applying the high magnetic field.

YbB_{12} is a canonical Kondo insulator and known to show clear insulator-metal (IM) transition at around 50 T [1]. At the field-induced IM phase transition, a steep increase of the magnetization also appears, and the phenomenon is often referred as metamagnetism or metamagnetic transition. The observed magnetization at 50 T, however, is smaller than half of the expected saturation magnetization. Higher magnetic fields are necessary to uncover the peculiar electronic and magnetic properties of YbB_{12} .

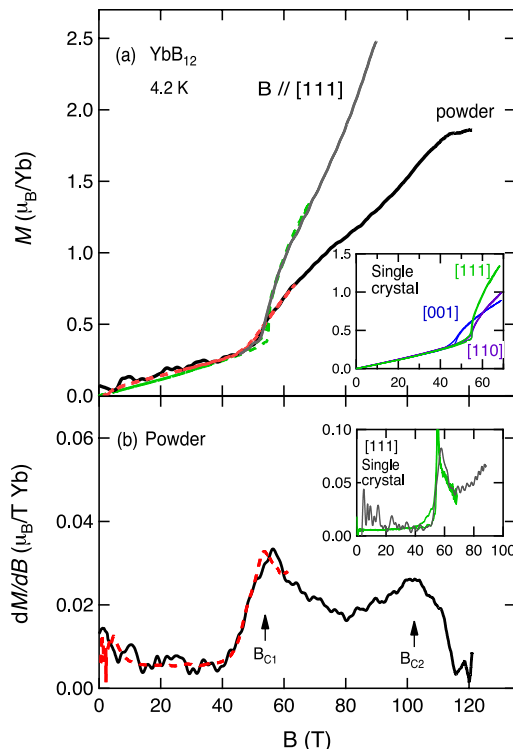


Fig. 1. (a) Magnetic field dependence of the magnetization (M) of YbB_{12} . The red-dashed and black-solid curves denote the magnetization of powder sample measured by a non-destructive pulsed magnet and that by HSTC, respectively. The green-dashed and gray-solid curves denote the M of a single crystal measured by a non-destructive pulse magnet and that using the HSTC, respectively. The inset shows the M curves of the single crystals with different magnetic field directions. (b) The field derivative of the magnetization (dM/dB) curves for the results of non-destructive pulse magnet (red-dashed curve) and that by the single-turn coil method (black solid curve). The inset shows dM/dB for the single crystal in the $B//[111]$ direction. The green-solid curve was obtained with a non-destructive magnet and the gray-solid curve was obtained with the HSTC.

Recently, we have conducted magnetization experiments on YbB_{12} in ultrahigh fields of up to 120 T. The horizontal-type single-turn coil (HSTC) is employed for the field generation. Figure 1 (a) shows the obtained magnetization curves; the thick black line and grey thin line represent the magnetization of the powdered sample and that of a single crystal, respectively. The magnetization curves of the single crystal with different directions of the applied magnetic field are shown in the inset of Fig. 1(a). In addition to the previously known metamagnetism around 50 T, another metamagnetic transition is observed in the powder sample at around 102 T [2]. This phenomenon is seen more clearly in the field variation of dM/dB (field derivative of the magnetization) as shown in Fig. 1(b). The metamagnetic transitions are observed as peak structures; there are broad but distinct two peaks at 55 and 102 T.

The observed successive two metamagnetic transitions can be interpreted as energy gap closing process. [1,2] In terms of the band magnetism, the metamagnetic transition occurs when the density of states (DOS) takes peak structure near Fermi energy at certain magnetic field. The two metamagnetic transitions indicate that there are multi-pseudo gap structures in the electronic state of YbB_{12} . Similar multi-pseudo gap structures have been suggested to exist in the Kondo semimetal CeNiSn [3], and the Kondo effect is theoretically predicted to collapse at the second metamagnetic transition when the larger pseudo-gap closes due to the Zeeman effect. Similar phenomenon probably takes place in YbB_{12} . The insulating state transforms to metallic state at around 50 T and the heavy fermion phase appears at magnetic fields in the range from 50 to 102 T. At higher fields exceeding 102 T, it is expected that the Kondo effect eventually vanishes and a normal metal state with saturated magnetization realizes. To validate this picture, further studies with single crystals are planned to be performed.

References

- [1] K. Sugiyama, F. Iga, M. Kasaya, T. Kasuya, and M. Date, J. Phys. Soc. Jpn. **57**, 3946 (1988).
- [2] T. T. Terashima, A. Ikeda, Y. H. Matsuda, A. Kondo, K. Kindo, and F. Iga, J. Phys. Soc. Jpn. **86**, 054710 (2017).
- [3] T. Yamada and Y. Ono, Phys. Rev. B **85**, 165114 (2012).

Authors

T. T. Terashima, A. Ikeda, Y. H. Matsuda, A. Kondo, K. Kindo, and F. Iga^a
^aIbaraki University

Solving the Mystery of the Topology of Semimetal Bismuth

I. Matsuda, Shin, and Komori Groups

Today, bismuth has become a central element in designing and in synthesizing topological materials such as $\text{Bi}_{1-x}\text{Sb}_x$, Bi_2Se_3 , and Na_3Bi . However, topology of the pure bismuth crystal has been still controversial. This is because the topology identification requires a precise determination of band structure of the bulk and edge-states of a material but the very small energy gap and the sharp dispersion have prevented from it even with recent photoemission spectroscopy techniques. In order to overcome the situation, we intentionally fabricated electronic interferometry in the bismuth films and combined with the ultrahigh-resolution measurement of angle-resolved photoemission spectroscopy ARPES [1].

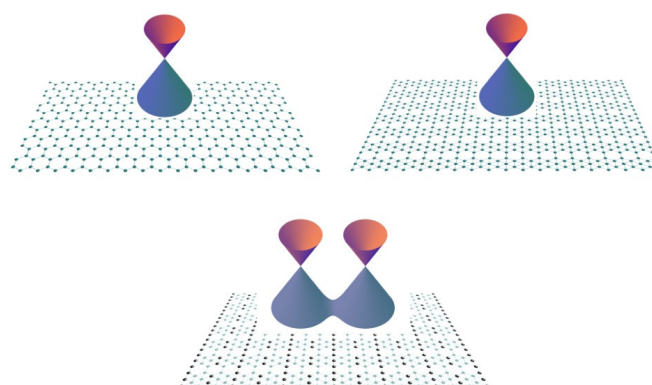
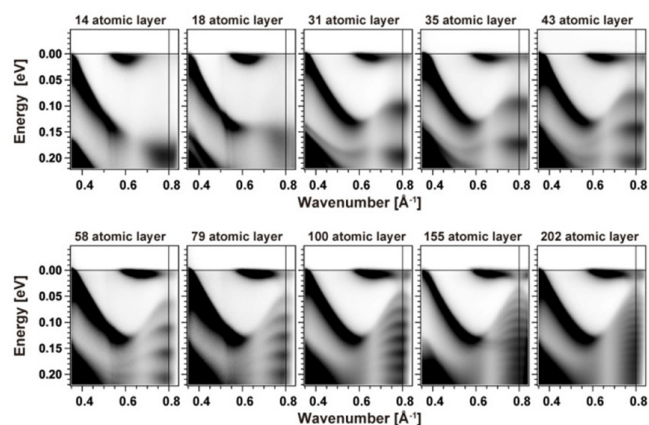


Fig. 1. Photoemission band diagrams of pure bismuth crystals measured at $h\nu=8.437$ eV. The film thickness is systematically increased from 14 to 202 atomic layer. An atomic layer corresponds to bilayer (BL), 1 BL=3.93 Å.

Figure 1 shows the ARPES results of the processed Bi crystals, normally a three-dimensional substance into an atomically thin two-dimensional film. The films were grown on the Ge(111) substrate. Electrons in a solid behave as electronic waves with a specific wavelength and energy. At all the thickness, a dispersion curve of the edge-state is observed at the Fermi level. On the other hand, at individual thickness, one can find different interference patterns of the electronic waves that are confined in the film. The systematic variation of the pattern allows us to determine the bulk band dispersion accurately. Then, from the precise electronic structures of the edge and the internal bulk, the pure bismuth crystal was unambiguously found to have the nontrivial topology, solving the long mystery [2].

References

- [1] S. Ito, B. Feng, M. Arita, A. Takayama, T. Someya, W.-C. Chen, C.-M. Cheng, C.-H. Lin, S. Yamamoto, T. Iimori, H. Namatame, M. Taniguchi, S.-J. Tang, F. Komori, K. Kobayashi, and I. Matsuda, *Phys. Rev. Lett.* **117**, 236402 (2016). (editor's choice).
 [2] Research highlight, *Nature Physics* **13**, 8 (2017).

Authors

S. Ito, Tai C. Chiang, F. Komori, and I. Matsuda

Fig. 1. (Upper) Dirac cones in the honeycomb lattice (graphene) and in the β_{12} -sheet structure (borophene). (Lower) A pair of Dirac cones in the periodically modulated β_{12} -sheet structure (borophene on Ag(111)).

band is actually forming a pair of Dirac cones by the high-resolution ARPES measurement using synchrotron radiation [2]. The borophene on Ag(111) forms the β_{12} -sheet structure and the theoretical calculations, the first principles and the tight-binding models, confirm presence of the Dirac cones. Moreover, by imposing the one-dimensional periodic potentials, the Dirac cones were found to form a pair, which completely reproduce the experimental bands. It is of note that the additional periodicity was confirmed by scanning tunneling microscope on the borophene. These results open the door to designing novel Dirac materials of the non-honeycomb structure and to make additional modification by the substrate that lead to varieties of functionalities (Fig. 1).

References

- [1] B. Feng, J. Zhang, Ro-Ya Liu, T. Iimori, C. Lian, H. Li, L. Chen, K. Wu, S. Meng, F. Komori, and I. Matsuda, *Phys. Rev. B* **94**, 041408(R) (2016).
 [2] B. Feng, O. Sugino, R.-Y. Liu, J. Zhang, R. Yukawa, M. Kawamura, T. Iimori, H. Kim, Y. Hasegawa, H. Li, L. Chen, K. Wu, H. Kumigashira, F. Komori, T.-C. Chiang, S. Meng, and I. Matsuda, *Phys. Rev. Lett.* **118**, 096401 (2017).

Authors

B. Feng, Tai C. Chiang, O. Sugino, F. Komori, and I. Matsuda

Dirac Fermions in Borophene

I. Matsuda, Sugino, and Komori Groups

Boron, the fifth element in the periodic table, has been known to be the lightest element substance that forms interatomic covalent bonds. Since the bonding states in the bulk boron range from two-center to multi-center bonds, boron forms varieties of allotropes that show rich physical and chemical properties. Up to now, all the allotropes of boron have been found to be semiconducting with a large band gap. Recently, the discovery of graphene has triggered great interest in the search for elemental monolayer materials and theoretical investigations have found existence of the monolayer boron, borophene, that shows metallicity.

In the present research, we synthesized a borophene by directly evaporating pure boron (99.9999%) onto a clean Ag(111) substrate. We apparently observed metallic boron-derived band by angle-resolved photoemission spectroscopy (ARPES). There are three pockets of the Fermi surfaces that are supported by the first-principles calculations [1]. Focusing onto a pair of the pockets, we discovered that the

Tailoring Photovoltage Responses at SrRuO₃/SrTiO₃ Heterostructures

I. Matsuda Group

Strontium titanate (SrTiO₃) has been one of the well-known transition-metal oxides and its perovskite crystal structure has enabled us to design a rich variety of metal-oxide heterostructures by epitaxial growth of oxide films. Recently, its photo-induced response has also attracted technological interests for usages of solar cells, photo diodes, photoelectrolysis, and photocatalysts. In such applications, the photovoltage effect is the most fundamental optical response and one needs to clarify the mechanism for designing and upgrading the systems. The surface photovoltage (SPV) effect is induced by photo-excitation, followed by spatial separations of carriers (holes and electrons) between the surface (interface) and the internal bulk. The effect is sensitive to the surface/interface band alignment and, thus, it is expected to improve the optical response by electronic design of the heterostructure.

By making element-selective time-resolved soft

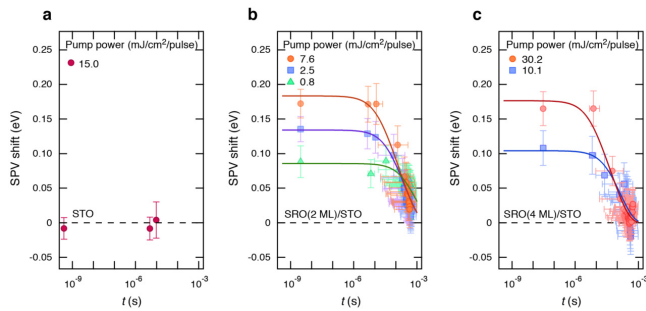


Fig. 1. Time dependence of the energy shifts of the surface photovoltage (SPV) effect after the optical pumping, traced by the time-resolved Sr 3d core-level photoemission measurements at a) SrTiO₃(STO), and b) SrRuO₃ (SRO)(2 ML)/ SrTiO₃ and c) SrRuO₃ (4 ML)/ SrTiO₃.

X-ray photoemission experiments at SPring-8 BL07LSU, we demonstrated that the photovoltage response can be enhanced in more than two orders of magnitude in SrTiO₃ by the epitaxial growth of 2 monolayer (ML) of SrRuO₃ thin film (0.8 nm), as shown in Fig.1. Moreover, we determined life-time of the photo-excited carriers in the perovskite heterostructures. Performance of the optical response matched with expectations from the band alignments. Our approach is fundamentally applicable for a variety of oxide heterojunctions and, therefore, it can be useful in fabricating the better opto-electronic devices such as high-efficient photo-detectors and solar cells.

References

[1] R. Yukawa, S. Yamamoto, K. Akikubo, K. Takeuchi, K. Ozawa, H. Kumigashira, and I. Matsuda, Adv. Mater. Interfaces **3**, 1600527 (2016).

Authors

R. Yukawa, S. Yamamoto, and I. Matsuda

Photoinduced Demagnetization and Insulator-to-Metal Transition in Ferromagnetic Insulating BaFeO₃ Thin Films

Wadati Group

Control of magnetic states by optical excitations in magnetically ordered materials has attracted considerable attention since the demonstration of ultrafast demagnetization in Ni within 1 ps, explored by time-resolved magneto-optical Kerr effect studies by Beaurepaire *et al.* [1]. They proposed a phenomenological “three-temperature model” in order to understand the ultrafast demagnetization, which considers three interacting reservoirs of electrons, spins, and

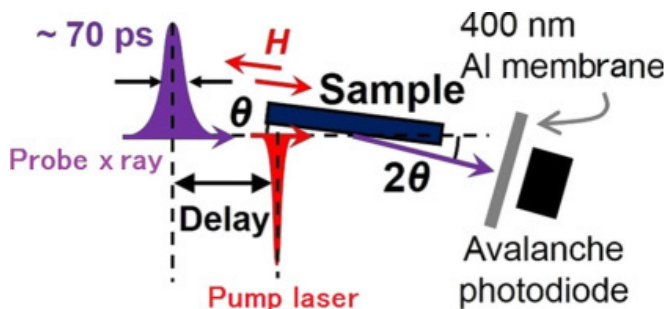


Fig. 1. Geometry of the measurements.

lattice, and suggested the importance of direct electron-spin interactions. Here we report on pump-probe time-resolved resonant x-ray reflectivity study of fully oxidized single crystalline BaFeO₃ thin films [2], which show unusual behaviors of ferromagnetic and insulating properties with saturation magnetization and a Curie temperature of 3.2 μ_B /formula unit and 115 K, respectively [3,4]. The investigation of the demagnetization dynamics of insulators allows one to relate electronic structure to magnetic dynamics.

In order to investigate the magnetic dynamics of ferromagnetic insulating BaFeO₃ thin films, we performed time-resolved reflectivity studies at the Femtospec slicing facility at the synchrotron radiation source BESSY II [5], using circularly polarized x-ray pulses. Our experimental method has the advantage that, in one reflectivity experiment, we can probe electronic structure as well as magnetism. The quality of the thin-film samples was confirmed by x-ray diffraction, Fe 2p x-ray absorption spectroscopy, and Fe 2p core-level hard x-ray photoemission spectroscopy measurements by comparing cluster-model calculations, which found that the formal valence of Fe was 4+ [3,4]. The experimental geometry is shown schematically in Fig. 1. We used fixed circular polarization and created magnetic contrast by switching the direction of the magnetic field (H), which was oriented along the sample surface ([010] direction). We recorded specular reflectivity data for two magnetization directions R⁺ and R⁻. The average reflectivity $R = (R^+ + R^-)/2$ is a measure of the electronic and structural properties, while the magnetic circular dichroism in reflectivity (MCDR) signal $DR = (R^+ - R^-)/2$ is a measure of the sample magnetization. A Ti:sapphire laser (wavelength: 800 nm, energy: 1.55 eV) with a pulse width of ~ 50 fs was employed as a pump laser with π polarization. The spot size of the pump laser was ~ 0.40 mm (horizontal) \times 0.25 mm (vertical), and that of the probe x ray was ~ 0.1 mm \times 0.1 mm. The repetition rate of the time-resolved measurement was 3 kHz, limited by the frequencies of the pump laser. The pumped and unpumped signals were obtained alternatively. The time resolution was 70 ps, corresponding to the pulse length of the probe x ray.

Figure 2(a) shows the time evolution of the MCDR intensities for different pump fluences. The vertical axis shows the excited MCDR intensities normalized by the unpumped signal (i.e., $\Delta R_{\text{pump}}/\Delta R_{\text{no pump}}$). Here, the subscript of pump and no pump denote the signals with and without the laser excitations, respectively. The MCDR intensities decrease after the incidence of the pump laser at $t = 0$. The time evolution of the MCDR intensity shows different behaviors with

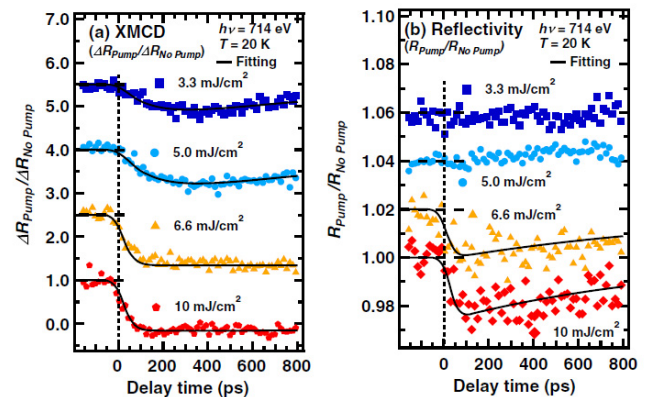


Fig. 2. Time evolution of (a) XMCD intensity and (b) reflectivity of BaFeO₃ thin films for various pump laser fluence. All the curves, except for the case of 10 mJ/cm², are shifted upward for clarity.

the change of the pump fluence (F). When F is smaller than 5.0 mJ/cm^2 , the demagnetization time is relatively slow and magnetization recovery sets in after about 400 ps. When the pump F is larger than 6.6 mJ/cm^2 , on the other hand, the demagnetization time is quite fast and no recovery of the magnetization can be observed within the first 800 ps. We assign the different behavior of the demagnetization dynamics to a laser-induced insulator-to-metal transition for $F \geq 6.6 \text{ mJ/cm}^2$, as discussed in the following. We show the time evolution of the intensity of the average reflectivity in Fig. 2(b), which allows us to investigate the electronic dynamics. The vertical axis shows the excited reflectivity intensities normalized by those without excitation (i.e., $R_{\text{pump}}/R_{\text{no pump}}$). No pump effects were observed for $F \leq 5.0 \text{ mJ/cm}^2$ with our time resolution of 70 ps. Pump effects, on the other hand, were clearly observed for $F \geq 6.6 \text{ mJ/cm}^2$.

Figure 3 shows the mechanism of the insulator-to-metal transition induced by the strong laser excitation. When the pump fluence is weaker than 5.0 mJ/cm^2 , magnetizations in BaFeO_3 thin films recover with the time constant of $\tau_{\text{recovery}} \sim 1000 \text{ ps}$. The time scale of $\sim 1000 \text{ ps}$ can be assigned to heat diffusion needed to cool the sample below the magnetic ordering temperature after electron, lattice, and spin systems have reached thermal equilibrium. Remarkably, the time-resolved reflectivity change for strong pump fluence also shows a recovery on this time scale of $\tau_{\text{recovery}} \sim 1000 \text{ ps}$, indicating that also here heat diffusion is the relevant mechanism. This latter observation is quite notable, because equilibrium between the electron and lattice temperature should be reached within 1 ps. The slow reopening of the band gap on time scales of $\sim 1000 \text{ ps}$ shows that for high excitation densities we drive the system into a metastable state. As a mechanism for the long lifetime of the metallic state, we consider that hot carriers, generated by the quasi-particle scattering and closing the band gap, prevent it from opening again by reducing electron-electron and electron-phonon interactions.

In summary, we investigated the electronic and magnetic dynamics by time-resolved reflectivity and MCDR measurement on BaFeO_3 thin films. When the pump laser fluence is smaller than 5.0 mJ/cm^2 , a relatively slow demagnetization of $\tau_{\text{decay}} \sim 150 \text{ ps}$ was observed, due to the insulating properties of the ground state in BaFeO_3 thin films without any changes in Fe 2p x-ray reflectivity. When the pump laser fluence is stronger than 6.6 mJ/cm^2 , on the other hand, rapid

changes in Fe 2p x-ray reflectivity are observed, which is attributed to a transition into a metallic state, resulting in an unusually fast demagnetization with $\tau_{\text{decay}} < 70 \text{ ps}$. Since BaFeO_3 thin films are near the phase boundary of a metal-insulator transition, the insulating phase is quite sensitive to carrier density. Thus, the origin of the insulator-to-metal transition is a photoinduced Mott transition into a metastable state stabilized by screened electron-electron and electron-phonon interactions. Our findings indicate a mechanism for tuning magnetic dynamics in correlated materials, which resembles heat-assisted magnetic switching in metallic magnets. By creating a sufficiently high excitation density, spin-flip scattering channels open up which increase the spin system susceptibility to external manipulation.

References

- [1] E. Beaurepaire, J.-C. Merle, A. Daunois, and J.-Y. Bigot, Phys. Rev. Lett. **76**, 4250 (1996).
- [2] T. Tsuyama, S. Chakraverty, S. Macke, N. Pontius, C. Schüßler-Langeheine, H.Y. Hwang, Y. Tokura, and H. Wadati Phys. Rev. Lett. **116**, 256402 (2016).
- [3] S. Chakraverty, T. Matsuda, N. Ogawa, H. Wadati, E. Ikenaga, M. Kawasaki, Y. Tokura, and H. Y. Hwang, Appl. Phys. Lett. **103**, 142416 (2013).
- [4] T. Tsuyama, T. Matsuda, S. Chakraverty, J. Okamoto, E. Ikenaga, A. Tanaka, T. Mizokawa, H. Y. Hwang, Y. Tokura, and H. Wadati, Phys. Rev. B **91**, 115101 (2015).
- [5] K. Hollack, J. Bahrtd, A. Balzer, U. Bovensiepen, M. Brzhezinskaya, A. Erko, A. Eschenlohr, R. Follath, A. Firsov, W. Frentrup, L. Le Guyader, T. Kachel, P. Kuske, R. Mitzner, R. Muller, N. Pontius, T. Quast, I. Radu, J.-S. Schmidt, C. Schüßler-Langeheine, M. Sperling, C. Stamm, C. Trabant, and A. Fohlisch, J. Synchrotron Radiat. **21**, 1090 (2014).

Authors

T. Tsuyama, S. Chakraverty^{b,c}, S. Macke^{d,e}, N. Pontius^f, C. Schüßler-Langeheine^f, H. Y. Hwang^{b,g,h}, Y. Tokura^{a,b}, and H. Wadatiⁱ
^aQuantum-Phase Electronics Center (QPEC), University of Tokyo
^bRIKEN Center for Emergent Matter Science (CEMS)
^cInstitute of Nano Science and Technology (INST)
^dQuantum Matter Institute, University of British Columbia
^eMax Planck Institute for Solid State Research
^fHelmholtz-Zentrum Berlin für Materialien und Energie GmbH
^gStanford Institute for Materials and Energy Sciences, SLAC National Accelerator Laboratory
^hStanford University

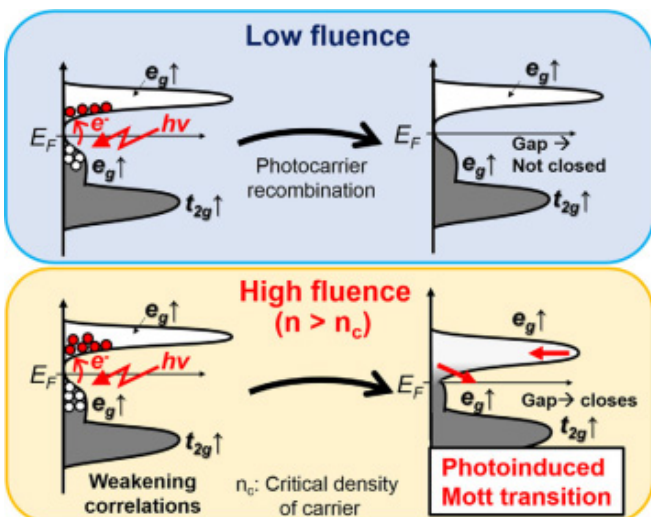


Fig. 3. Mechanism of the insulator-to-metal transition induced by the strong laser excitation.

